


Article

Model-Based Analysis for Ethylene Carbonate Hydrogenation Operation in Industrial-Type Tubular Reactors

Hai Huang¹, Chenxi Cao^{2,*} , Yue Wang³, Youwei Yang³, Jianning Lv⁴ and Jing Xu^{1,5,*}

¹ State Key Laboratory of Chemical Engineering, School of Chemical Engineering, East China University of Science and Technology, Shanghai 200237, China; haielvis@163.com

² Key Laboratory of Smart Manufacturing in Energy Chemical Process, Ministry of Education, East China University of Science and Technology, Shanghai 200237, China

³ Key Laboratory for Green Chemical Technology of Ministry of Education, Collaborative Innovation Center of Chemical Science and Engineering, School of Chemical Engineering and Technology, Tianjin University, Tianjin 300072, China; yuewang@tju.edu.cn (Y.W.); yangyouwei@tju.edu.cn (Y.Y.)

⁴ Wison Engineering Ltd., 633 Zhongke Rd., Shanghai 201210, China; lvjianning@wison.com

⁵ Guangxi Key Laboratory of Petrochemical Resource Processing and Process Intensification Technology, School of Chemistry and Chemical Engineering, Guangxi University, Nanning 530004, China

* Correspondence: caocx@ecust.edu.cn (C.C.); xujing@ecust.edu.cn (J.X.)

Abstract: Hydrogenation of ethylene carbonate (EC) to co-produce methanol (MeOH) and ethylene glycol (EG) offers an atomically economic route for CO₂ utilization. Herein, aided with bench and pilot plant data, we established engineering a kinetics model and multiscale reactor models for heterogeneous EC hydrogenation using representative industrial-type reactors. Model-based analysis indicates that single-stage adiabatic reactors, despite a moderate temperature rise of 12 K, suffer from a narrow operational window delimited by EC condensation at lower temperatures and intense secondary EG hydrogenation at higher temperatures. Boiling water cooled multi-tubular reactors feature near-isothermal operation and exhibit better operability, especially under high pressure and low space velocity. Conduction oil-cooled reactors show U-type axial temperature profiles, rendering even wider operational windows regarding coolant temperatures than the water-cooled reactor. The revelation of operational characteristics of EC hydrogenation under industrial conditions will guide further improvement in reactor design and process optimization.

Keywords: ethylene carbonate hydrogenation; methanol; ethylene glycol; multiscale reactor model; reactor analysis; operation window



Citation: Huang, H.; Cao, C.; Wang, Y.; Yang, Y.; Lv, J.; Xu, J. Model-Based Analysis for Ethylene Carbonate Hydrogenation Operation in Industrial-Type Tubular Reactors. *Processes* **2022**, *10*, 688. <https://doi.org/10.3390/pr10040688>

Academic Editor: Blaž Likozar

Received: 21 March 2022

Accepted: 28 March 2022

Published: 31 March 2022

Publisher's Note: MDPI stays neutral with regard to jurisdictional claims in published maps and institutional affiliations.



Copyright: © 2022 by the authors. Licensee MDPI, Basel, Switzerland. This article is an open access article distributed under the terms and conditions of the Creative Commons Attribution (CC BY) license (<https://creativecommons.org/licenses/by/4.0/>).

1. Introduction

Efficient chemical conversion and utilization of CO₂ is envisioned as an important vector in future carbon-neutral and carbon-negative human society [1,2]. Researchers are in hot pursuit of disposing the energy- and industry-related CO₂ emissions by renewable electricity or discarded H₂ to produce feedstock or commodity chemicals [3–5]. In particular, thermo-/electro-chemical CO₂ reduction to oxygenates, for instance, aldehydes, alcohols, and carboxyl acids, exerts great prospects in high-atom-economy CO₂-based chemical manufacture by reducing the by-production of H₂O [6–10]. Direct hydrogenation of CO₂ into methanol (MeOH) has attracted intense research attention in recent years in that MeOH serves as a commodity chemical as well as a crucial platform to various downstream products [11–15]. However, this process is inherently limited by the kinetic inertness and thermodynamic stability of the CO₂ molecule, resulting in extremely low per-pass CO₂ conversion (~10~20%), and thereby a poor atom economy [16–18].

A feasible solution to by-pass the thermodynamic limitation is to “bridge” the low-energy CO₂ reactant and the high-energy MeOH product with a CO₂-derivable, medium-energy intermediate, such as ethylene carbonate (EC), dimethyl carbonate, methyl formate,

and so on [19–23]. Such indirect green methanol production processes are advantageous in milder reaction conditions as well as higher per-pass CO₂ conversion (over 95%) and overall methanol yield. Amongst these processes, EC hydrogenation as illustrated in Figure 1 is of great interest:

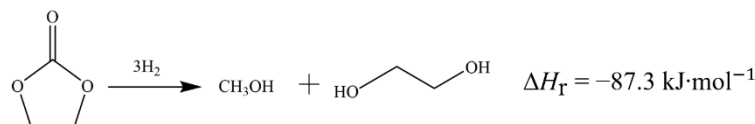


Figure 1. EC hydrogenation reaction.

This process co-produces methanol and ethylene glycol (EG), another value-added bulk chemical, with theoretically 100% atom economy. In addition, EC production using CO₂ and ethylene oxide has already been demonstrated [24,25], making the subsequent EC hydrogenation process a promising enabler for industrially relevant green alcohols production.

Development of catalyst systems for EC hydrogenation has gained considerable progress. Since Han et al. [26] first proposed a Ru II PNP catalyst for homogeneous EC hydrogenation, the catalyst system has evolved from homogeneous noble metal complex [27] to heterogeneous supported copper (Cu) based catalysts [28–33], in view of difficult separation and recovery of the former and, in contrast, convenient deployment of the latter. As the early-version Cu-based catalysts are inferior to the homogeneous catalysts in performance, continuous efforts are being paid to develop more active and selective candidates suitable for industrial application [34–36]. Song et al. [37] prepared MoO_x-promoted Cu/SiO₂ catalyst, which achieved 89% MeOH yield and 99% EG yield within 150 h time-on-stream at a H₂/EC ratio of 20 and a WLHSV (weight liquid hourly space velocity of EC) of 0.64 g_{EC}·g_{cat}⁻¹·h⁻¹. Carbon modified Cu catalyst proposed by Chen et al. [38] displayed good activity and stability after using for 264 h, owing to improved dispersion of Cu particles, showing EC conversion of 100%, and EG and MeOH selectivities up to 99.9% and 85.8%, respectively. Appropriate synergy between Cu⁰ and Cu⁺ species are believed to play an important role in the activation of H₂, providing adsorption sites for the carbonyl groups of EC, and stabilizing the surface acyl and methoxy species, leading to improved EC conversion and alcohol yields [39,40].

Despite the progress in catalyst investigation, to date, the heterogeneous EC hydrogenation process has not been studied at a pilot scale. Tailoring the transport characteristics of industrial-scale reactors in accordance with the intrinsic reaction kinetics is crucial for commercial operation of catalytic processes [41,42]. In this respect, industrial methanol synthesis serves as a reference given a similar reaction enthalpy change and the employment of similar Cu-based catalysts. Multi-stage adiabatic fixed bed reactors and boiling water-cooled multi-tubular reactors are the most commonly applied types of reactors in methanol synthesis [42]. The design and operation optimization of these reactors has been well aided by model-based analysis accounting for intrinsic reaction kinetics, internal/external mass transfer at the scale of catalyst particles, and heat and mass transfer at the reactor-scale [43]. Recently, Samimi et al. [44] compared water cooled, gas cooled, and double cooled reactors for direct CO₂ hydrogenation to MeOH by one-dimensional reactor models focusing on the phase stability. The gas cooled reactor exhibits the lowest possibility of methanol condensation and the highest methanol yield. Cui et al. [45] assessed the potentials of adiabatic, water cooled and gas cooled reactors for direct CO₂ hydrogenation to MeOH using coupled two-dimensional (2D) computational fluid dynamics (CFD) models for the reactor and single catalyst particles. The water-cooled reactors demonstrate outstanding temperature control at the expense of a higher capital cost. It is apparent that, to promote the process towards commercialization, understanding of the operational behaviors of EC hydrogenation in industrial-type reactors is urgently needed.

Herein, we investigated the operational characteristics of industrial-type adiabatic, water-cooled and oil-cooled tubular reactors for a 3 × 10⁴ t/a EC hydrogenation process

by model-based comparative analysis. Two-dimensional (2D) pseudo-homogeneous CFD models were established with engineering kinetic models developed for heterogeneous EC hydrogenation over an industrial Cu-based catalyst, and validated by bench-scale and pilot-scale reaction data. The operation windows of key reactor operating variables, including reactant/coolant inlet temperature, total pressure and space velocity, were delineated for the representative industrial-type reactors, considering both the reactor performance and the EC phase change boundaries. The presented results will pave the way to future industrial design and optimization of reactors and process for the green alcohols production.

2. Methods

2.1. Method Description

Figure 2 illustrates the industrial reactors for ethylene carbonate hydrogenation considered and the modeling scheme used in this study. Two types of industrial reactors are modeled, namely, adiabatic and multi-tubular heat-exchange reactors; for the heat-exchange reactors, two different coolants are considered: boiling water and heat conduction oil (Figure 2a). The adiabatic reactor is 2 m in diameter and 8 m in length, whereas the heat-exchange reactor comprises 1682 tubes of 0.05 m diameter and 8 m length, corresponding to a total capacity of 3×10^4 t/a methanol and ethylene glycol. Key geometric parameters and operating conditions are listed in Table 1. The 2D asymmetrical steady-state multi-scale reactor models are built under the following assumptions:

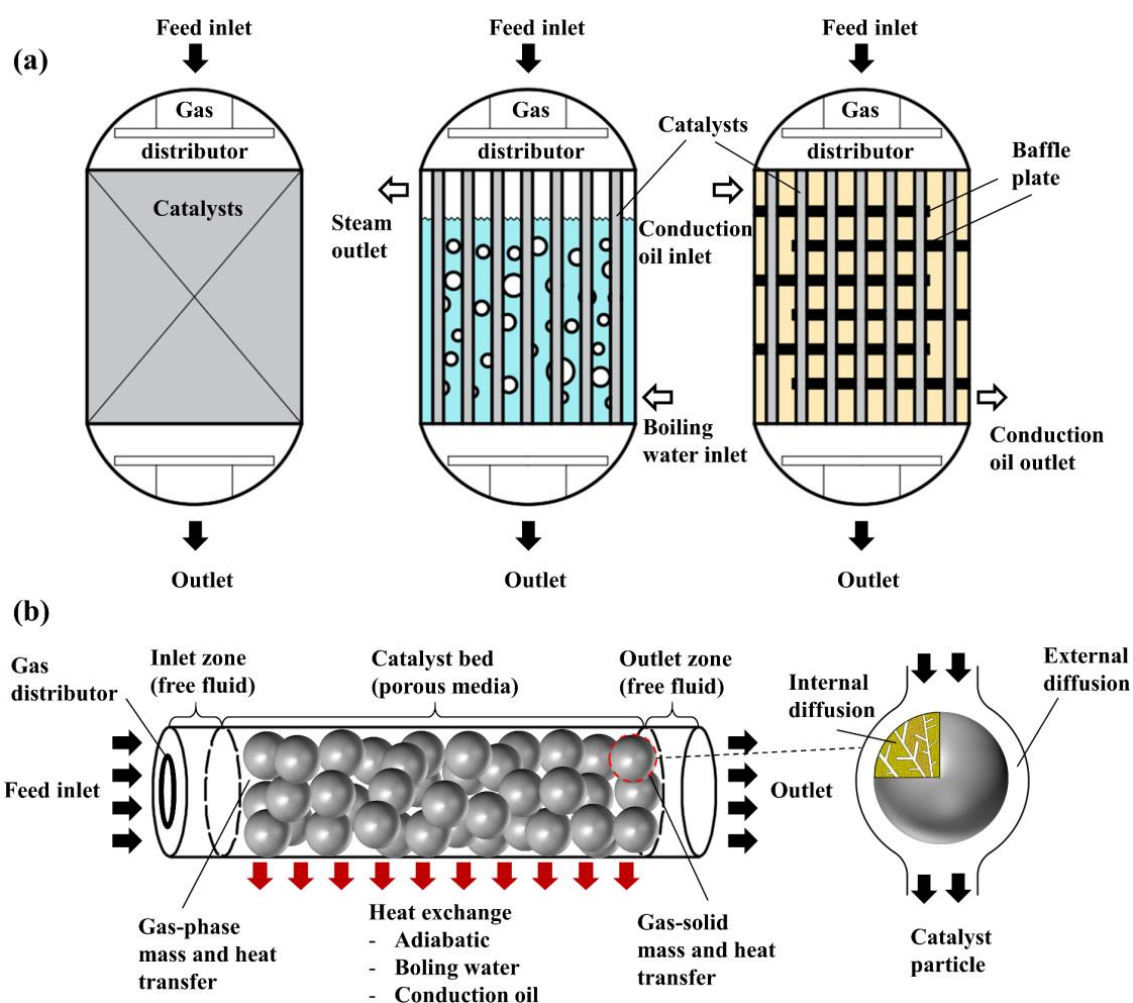


Figure 2. Schematic diagram of (a) industrial adiabatic and heat-exchange reactors for ethylene carbonate hydrogenation and (b) the multi-scale reactor model.

Table 1. Model parameters.

Geometric Parameters	Adiabatic FBR	Heat-Exchange FBR
Bed/Tube diameter, D (m)	2	0.05
Developing zone length		2 m
Reaction zone length		8 m
Catalyst type		Cu/SiO ₂ [30]
Catalyst geometry	3/5/7 mm (sphere); 3 × 3/5 × 5/7 × 7 mm (cylinder)	
Catalyst loading mass (kg)	13730 kg for (5 mm sphere)	
Average bed voidage	0.4 (5 mm sphere)	0.43 (5 mm sphere)
Gas distributor geometry	1 m diameter, ring	/
Operating conditions (Nominal value/range)		
Temperature, T_{in} (K)		463/433–483
Coolant temperature, T_c (K)	/	463/423–463
Pressure, P_{op} (MPa)		3/1–5
Space velocity, SV (g _{EC} · g _{cat} ⁻¹ · h ⁻¹)		0.3/0.1–0.5
Molar ratio of H ₂ to EC		200/80–200

Details of the multi-scale reactor models, including governing equations, heat and mass transfer correlations, chemical kinetics and model implementation are introduced in the following text.

1. Reactants are fed into the adiabatic reactor through inlet manifolds, which are simplified into a ring.
2. The inlet gas distributor of the heat-exchange multi-tubular reactor ensures uniform distribution of the reactants to all reaction tubes, so that only a single reaction tube is modeled as representative.
3. The wall temperatures of all reaction tubes of the boiling water-cooled reactor are equal to the boiling temperature of pressurized water.
4. The coolant temperature and external heat transfer coefficient are the same for all reaction tubes of the oil-cooled reactor.

2.2. Governing Equations

The fluid computational mass conservation equation in the bed is

$$\frac{\partial(\varepsilon_b \rho_f)}{\partial t} + \nabla \cdot (\varepsilon_b \rho_f \mathbf{v}) = 0 \quad (1)$$

The momentum Equation (2), the energy Equation (7) and the species transport equation Equation (10) for flow in the catalyst bed are listed below.

Momentum equation:

$$\frac{\partial(\varepsilon_b \rho_f \mathbf{v})}{\partial t} + \nabla \cdot (\varepsilon_b \rho_f \mathbf{v} \mathbf{v}) = -\varepsilon_b \nabla p + \nabla \cdot (\varepsilon_b \boldsymbol{\tau}) + S_\phi \quad (2)$$

where p is the static pressure and $\boldsymbol{\tau}$ is the stress tensor. S_ϕ is the momentum source term for fluid flow in porous media,

$$S_\phi = \mathbf{B}_f - \left(\frac{\varepsilon_b^2 \mu}{K} \mathbf{v} + \frac{\varepsilon_b^3 C_2}{2} \rho_f |\mathbf{v}| \mathbf{v} \right) \quad (3)$$

representing the viscous and inertial drag forces imposed on the fluid flow by the pore walls within the porous media, in which C_2 is the inertial loss coefficient.

$$C_2 = \frac{3.5 (1 - \varepsilon_b)}{d_p^v \varepsilon_b^3} \quad (4)$$

The k - ω SST turbulence model is used with the turbulence kinetic energy k and the specific dissipation rate ω obtained from the following equations:

$$\frac{\partial(\rho_f k)}{\partial t} + \frac{\partial(\rho_f k u_i)}{\partial x_i} = \frac{\partial}{\partial x_j} \left(\Gamma_k \frac{\partial k}{\partial x_j} \right) + G_k - Y_k + S_k + G_{kb} \quad (5)$$

$$\frac{\partial(\rho_f \omega)}{\partial t} + \frac{\partial(\rho_f \omega u_i)}{\partial x_i} = \frac{\partial}{\partial x_j} \left(\Gamma_\omega \frac{\partial \omega}{\partial x_j} \right) + G_\omega - Y_\omega + S_\omega + G_{\omega b} \quad (6)$$

Energy equation:

$$\begin{aligned} \frac{\partial}{\partial t} (\varepsilon_b \rho_f E_f + (1 - \varepsilon_b) \rho_s E_s) + \nabla \cdot (\mathbf{v} (\rho_f E_f + p)) \\ = S_f^h + \nabla \cdot [k_e \nabla T - (\sum_i h_i J_i) + (\boldsymbol{\tau} \cdot \mathbf{v})] \end{aligned} \quad (7)$$

where E_f is total fluid energy and E_s is total solid medium energy. The energy source S_f^h represents the chemical reaction heat.

$$S_f^h = - \sum_j \frac{h_j^0}{M_{w,j}} R_j \quad (8)$$

where h_j^0 is the enthalpy of formation of species and R_j is the volumetric rate of creation of species j . The effective heat conduction of bed k_e is computed in Equation (9).

$$k_e = \begin{cases} k_{e,ax} = \frac{u_0 \rho_f c_p d_p^2}{Pe_{h,ax}} \\ k_{e,r} = \frac{k_r^0}{k_f} + k_f \cdot \frac{Pe_{h,r}^0}{Pe_{h,r}} \end{cases} \quad (9)$$

Species equation:

$$\frac{\partial}{\partial t} (\rho_f Y_i) + \nabla \cdot (\rho_f \mathbf{v} Y_i) = -\nabla \cdot \mathbf{J}_i + S_i \quad (10)$$

where Y_i is mass fraction of each species, and \mathbf{J}_i is the diffusive flux of species i arising from gradients of species concentration and temperature.

$$\mathbf{J}_i = -\rho_f D_e \sum_{j=1}^{N-1} \nabla Y_j - D_{T,i} \frac{\nabla T}{T} \quad (11)$$

S_i , the net source of species i due to chemical reactions, S_i is computed as the sum of the reaction rates:

$$S_i = M_{w,i} \sum_{r=1}^{N_R} \hat{R}_{i,r} \quad (12)$$

where $M_{w,i}$ is the molecular weight of species i and $\hat{R}_{i,r}$ is the molar rate of creation/destruction of species i in reaction r . In Equation (11), the calculation of thermal diffusion coefficients $D_{T,i}$ adopts the following empirically based expression [46].

$$D_{T,i} = -2.59 \times 10^{-7} T^{0.659} \left[\frac{M_{w,i}^{0.511} X_i}{\sum_{i=1}^N M_{w,i}^{0.511} X_i} - Y_i \right] \cdot \left[\frac{\sum_{i=1}^N M_{w,i}^{0.511} X_i}{\sum_{i=1}^N M_{w,i}^{0.489} X_i} \right] \quad (13)$$

where X_i is mole fraction of species i ; the effective mass transfer coefficient of bed D_e is computed as:

$$D_e = \begin{cases} D_{e,ax} = \frac{d_p^2 u_0}{Pe_{m,ax}} \\ D_{e,r} = \frac{d_p^2 u_0}{Pe_{m,r}} \end{cases} \quad (14)$$

2.3. Bed Voidage and Pressure Drop

When the ratio of tube diameter to the catalyst's volume-equivalent diameter (denoted by R in the following paper) is less than 10, the wall effect cannot be ignored [47]. In this work, R values for the adiabatic fixed bed (2 m in diameter) and the heat-exchange reactor (single tube 0.05 m in diameter) filled with 5 mm spherical catalyst are 400 and 10, respectively. Therefore, without the wall effect, the bed voidage of the adiabatic reactor is set as constant in the radial direction (Supplementary Materials Table S5). Meanwhile, the fluctuations of bed voidage in the radial direction is considered for the heat-exchange reactors (Table S5) [48–50].

The bed pressure drop is computed by the Ergun equation in Equation (15) [51].

$$\frac{|\Delta P|}{L} = \frac{150}{d_p^2} \frac{(1 - \varepsilon_b)^2 \mu}{\varepsilon_b^3} u_0 + \frac{1.75 \rho_f (1 - \varepsilon_b)}{d_p^2 \varepsilon_b^3} u_0^2 \quad (15)$$

2.4. Heat and Mass Transfer in the Catalyst Bed

The axial effective heat conduction is computed as [52]:

$$k_{e,ax} = \frac{u_0 \rho_f c_{p,f} d_p^V}{Pe_{h,ax}} \quad (16)$$

in which the Peclet number for axial heat conduction $Pe_{h,ax}$ equals 2.

The radial effective heat conduction is computed by:

$$k_{e,r} = \frac{k_r^0}{k_f} + k_f \frac{Pe_h^0}{Pe_{h,r}^\infty} \quad (17)$$

in which the molecular Peclet number Pe_h^0 is [53]:

$$Pe_h^0 = RePr = \frac{u_0 \rho_f c_{p,f} d_p^V}{k_f} \quad (18)$$

and $Pe_{h,r}^\infty$ is [54]:

$$Pe_{h,r}^\infty = 8 \left[2 - \left(1 - \frac{2}{R} \right)^2 \right] \quad (19)$$

The following expression for the effective thermal stagnant conductivity $\frac{k_r^0}{k_f}$ is obtained by Equation (20) [55]:

$$\frac{k_r^0}{k_f} = (1 - \sqrt{1 - \varepsilon_b}) + \frac{2\sqrt{1 - \varepsilon_b}}{1 - B\kappa^{-1}} \times \left[\frac{B(1 - \kappa^{-1})}{(1 - B\kappa^{-1})^2} \ln\left(\frac{\kappa}{B}\right) - \frac{B-1}{1 - B\kappa^{-1}} - \frac{B+1}{2} \right] \quad (20)$$

where $B = C_f \left(\frac{1 - \varepsilon_b}{\varepsilon_b} \right)^{1.11}$; $C_f = 1.25$ (sphere), $C_f = 2.5$ (cylinder).

Under turbulent conditions ($Re > 100$), axial mixing of mass can be approximated as mixing in a cascade of L/d_p ideal mixers [56]. The Peclet number for axial mass dispersion approximately equals 2.

$$Pe_{m,ax} = \frac{d_p^V u_0}{D_{e,ax}} = 2 \quad (21)$$

The effective radial mass transfer coefficient of bed $D_{e,r}$ is computed as [57]:

$$Pe_{m,r} = \frac{d_p^V u_0}{D_{e,r}} = C \left(1 + \frac{19.4}{R^2} \right) \quad (22)$$

where $C = 8.65 \frac{d_p^v}{d_p^a}$ [58].

2.5. Heat and Mass Transfer of Catalyst Particles

Due to mild exothermicity of the ethylene carbonate hydrogenation reaction, the temperature difference between the catalyst surface and the gas phase is estimated to be less than 1 K in Equation (23). Consequently, the temperature of catalyst surface and the gas phase is taken as identical. The gas–solid heat transfer coefficient α_f is calculated as [59]:

$$\Delta T_{\text{ex}} = \frac{Q_{\text{reaction}}}{\alpha_f \cdot S_{\text{cat}}} \quad (23)$$

$$Nu = 2 + 1.1Re^{0.6} \cdot Pr^{\frac{1}{3}} \quad (24)$$

$$Nu = \frac{\alpha_f d_p^v}{k_f} \quad (25)$$

For heat transfer inside the catalyst particle, the temperature gradient within the catalyst particle is related to the heat of reaction Q_{reaction} and the effective thermal conductivity of the catalyst particle $\lambda_{\text{eff,cat}}$ (Equation (26)) and can be calculated by Equation (27) [60,61].

$$\Delta T_{\text{in}} = \frac{D_{\text{eff,EC}} \cdot (C_{\text{EC,s}} - C_{\text{EC,center}}) \cdot (-\Delta_r H)}{\lambda_{\text{eff,cat}}} \quad (26)$$

$$\lambda_{\text{eff,cat}} = k_f \left(\frac{k_s}{k_f} \right)^{1-\epsilon_{\text{cat}}} \quad (27)$$

Under the reaction conditions considered in this article, ΔT_{in} is estimated to be less than 1 K. Therefore, the catalyst particle is considered isothermal.

The mass transfer between the catalyst surface and the gas phase is described by a mass transport coefficient k_g :

$$k_g \cdot a \cdot (C_{\text{EC,gas}} - C_{\text{EC,s}}) = R_{\text{EC,s}} \quad (28)$$

where $R_{\text{EC,s}}$ is the effective consumption rate of EC at the particle surface. k_g is related to the catalyst shape, the Reynolds number and the Schmidt number, as shown in Equations (29)–(31) [62].

$$Sh = 2 + 0.6Re^{0.5} Sc^{\frac{1}{3}} \quad (\text{sphere}) \quad (29)$$

$$Sh = 0.61Re^{0.5} Sc^{\frac{1}{3}} \quad (\text{cylinder}) \quad (30)$$

$$Sh = \frac{k_g d_p^v}{D_{\text{EC,m}}} \quad (31)$$

The effect of mass transfer inside the catalyst particles, namely, internal mass transfer, is accounted for with the generalized Thiele modulus approach, which is applicable to a broad range of rate equations [63]. The generalized Thiele modulus with respect to EC consumption rate ($\phi_{\text{gen,EC}}$) is expressed as

$$\phi_{\text{gen,EC}} = \frac{V_{\text{cat}}}{S_{\text{cat}}} \sqrt{\frac{k_v}{D_{\text{eff,EC}}} \cdot \frac{n+1}{2} \cdot C_{\text{EC,s}}^{n-1}} \quad (32)$$

The effectiveness factor for internal mass transfer is then computed as:

$$\eta_{\text{EC}} = \frac{\tanh(\phi_{\text{gen,EC}})}{\phi_{\text{gen,EC}}} \quad (33)$$

Note that Equations (28)–(31) must be solved simultaneously in an iterative manner because the two sides in Equation (28) are related by the EC concentration at catalyst particle surface, which is unknown in advance.

2.6. Coolant Heat Transfer

For the heat exchange by pressurized boiling water, a large heat transfer coefficient (4000–6000 W·m⁻²·K⁻¹) and a constant wall temperature (T_w) are considered:

$$T_w = T_b \quad (34)$$

where T_b is the boiling point of pressurized water.

In contrast, the heat conduction oil has a low specific heat capacity, and thus is heated up easily. The oil temperature is therefore considered as a function of the transferred heat. The oil-to-tube heat transfer coefficient is set as a function of the space in between adjacent baffle plates t and the coolant mass flow rate \dot{m}_{oil} .

$$\alpha_{oil} = \bar{\alpha}_{oil}(t, \dot{m}_{oil}) \quad (35)$$

The detailed expressions are given in the Supporting Information. The heat transferred between the oil and the tube wall is

$$Q_{oil} = \bar{\alpha}_{oil} \cdot (T_{oil} - T_w) \cdot S_{wall} \quad (36)$$

As the oil temperature T_{oil} varies with the axial position, the steady-state coolant temperature profile is determined by iteration. The single reaction tube is divided into 10 segments (each 0.8 m long) in the flow direction with the oil temperature in each segment calculated as

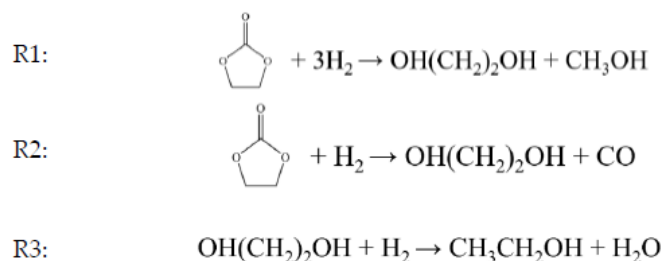
$$T_{oil,i+1} = \begin{cases} T_{oil,in}, & i = -1 \\ T_{oil,i} + \frac{Q_{oil,i}}{3600c_{p,oil} \cdot \dot{m}_{oil}}, & 0 \leq i \leq 9 \end{cases} \quad (37)$$

when the iteration converges, the oil temperature as a continuous function of the axial position is calculated by linear interpolation of the above discrete temperatures.

$$T_{oil}(x) = T_{oil,i-1} + \frac{T_{oil,i} - T_{oil,i-1}}{x_i - x_{i-1}} \cdot (x - x_{i-1}), \quad (x_{i-1} < x < x_i) \quad (38)$$

2.7. Chemical Reactions

The global reaction of ethylene carbonate hydrogenation to ethylene glycol and methanol is described by three separate reactions as shown in (R1)–(R3), respectively. This scheme allows for investigation of the effect of operating variables on the reactant conversion and product selectivity. The intrinsic kinetics of these reactions are modeled by power-law equations. The kinetic parameters were fitted to bench-scale experimental data covering a wide range of reaction conditions of $T = 175$ – 220 °C, $P_{op} = 3.0$ MPa, $H_2/EC = 120$ – 200 and $SV = 0.5$ – 2.2 h⁻¹. Details regarding the kinetic equations and parameters are given in the Supporting Information (Section S1).



Since the two EC hydrogenation reactions ((R1) and (R3)) are dependent on the gas phase EC concentration only, their effective reaction rates over the catalyst particle surface are:

$$r_{\text{obs}} = \eta_{\text{EC}} \cdot r_{\text{chem}}(C_{\text{EC},s}, T_s) \quad (39)$$

The EG hydrogenation reaction (R3) is zeroth order; therefore, its effective reaction rate is equal to the intrinsic reaction rate:

$$r_{\text{obs}} = r_{\text{chem}}(C_{\text{EG},s}, T_s) \quad (40)$$

The performance metrics of the reaction, EC conversion X_{EC} , EG selectivity S_{EG} , MeOH selectivity S_{MeOH} and total alcohols selectivity S_{Alcohol} , are defined by the following definitions:

$$X_{\text{EC}} = \frac{\dot{m}_{\text{EC},\text{in}} - \dot{m}_{\text{EC},\text{out}}}{\dot{m}_{\text{EC},\text{in}}} \quad (41)$$

$$S_{\text{EG}} = \frac{\dot{m}_{\text{EG},\text{out}}/M_{\text{EG}}}{(\dot{m}_{\text{EC},\text{in}} - \dot{m}_{\text{EC},\text{out}})/M_{\text{EC}}} \quad (42)$$

$$S_{\text{MeOH}} = \frac{\dot{m}_{\text{MeOH},\text{out}}/M_{\text{MeOH}}}{(\dot{m}_{\text{EC},\text{in}} - \dot{m}_{\text{EC},\text{out}})/M_{\text{EC}}} \quad (43)$$

$$S_{\text{Alcohol}} = \frac{S_{\text{EG}} + S_{\text{MeOH}}}{2} \quad (44)$$

2.8. Model Implementation

The multi-scale reactor models were implemented in the FLUENT software. The computational domains were discretized using rectangular meshes refined in the inlet regions and adjacent to the walls. Spatial discretization was conducted by the second-order upwind differencing scheme. The pressure–velocity coupling was performed with the SIMPLEC algorithm. User defined function (UDF) of FLUENT was used to couple the heat and mass transport models and chemical kinetics to the reactor-level models. The inlet boundary was set as uniform velocity. The outlet boundary was set as constant pressure (operating pressure) and zero normal gradients of velocity, temperature and species mass fractions. A no-slip, adiabatic or thermally coupled boundary was imposed on the reactor walls depending on the reactor type. Axisymmetric boundaries were imposed on the centerline of the reactor. The convergence criteria were set as all residuals below 10^{-3} . Simulations were performed on PC with Intel i9-9900X processors (Intel Corporation, Santa Clara, CA, USA) and 64 GB RAM (G.skill International Enterprise Co., Ltd., Taipei, China). The typical computation time under each operating condition is between 0.5 and 2 h.

3. Results and Discussion

3.1. Model Validation

Table 2 shows results of the grid independence study using EC conversion as the most sensitive key variable. When the grid size exceeds 10,000, the EC conversions remain unchanged for both adiabatic and heat-exchange reactor models with sphere/cylinder catalysts. Therefore, the following work was carried out with a grid size of 10,000.

To validate the established multi-scale reactor and chemical kinetics model, we compared the model predictions with pilot plant data. The EC hydrogenation pilot reactor was operated at a production capacity of 1000 t_{alcohol}/a and had steadily run for over 72 h to allow collection of all reaction products. The structure and working conditions of the pilot reactor are shown in Table 3. Simulations were conducted with the same parameter settings as the pilot reactor, including the reactor geometry, operating conditions and catalyst properties. Figure 3 shows the mass flow rates of the converted EC and the produced EG, MeOH and by-products measured in pilot plant run and those predicted by our model. The model predictions are in quantitative agreement with the pilot plant data with relative

errors for both the converted EC and the produced EG < 5%. The amount of produced MeOH is underestimated by ~20%, which is accompanied by an overestimated amount of by-products. The reason is suspected to be incomplete measurement of the volatile MeOH in bench-scale experiments used for deriving the kinetics parameters. Nonetheless, the multi-scale reactor model is reliable in predicting the generic reaction performance of EC hydrogenation in industrial reactors and will be used to explore the operational behaviors of different types of tubular reactors.

Table 2. Dependence of EC conversion on grid sizes in simulation.

Adiabatic Reactor Model				
Mesh Size		1250	10,000	20,000
EC conversions (%)	20% length (sphere)	37.6	39.0	39.1
	outlet (sphere)	94.1	94.0	94.0
	20% length (cylinder)	29.7	30.2	30.1
	outlet (cylinder)	86.0	85.1	84.8
Heat-Exchange Reactor Model				
Mesh Size		2500	10,000	40,000
EC conversions (%)	20% length (sphere)	36.8	38.0	38.3
	outlet (sphere)	93.2	93.2	93.2
	20% length (cylinder)	33.7	34.8	35.1
	outlet (cylinder)	89.4	89.4	89.4

Table 3. Structure and working conditions of the pilot reactor for EC hydrogenation.

Pilot Reactor Configuration	
Tube Inner Diameter (m)	0.034
Tube length (m)	4
Tube number	95
Operating Conditions	
EC mass flow ($\text{kg}\cdot\text{h}^{-1}$)	107.3
Feed EC to H_2 molar ratio	170
Feed temperature (K)	458.2
Coolant type	Conduction oil
Coolant mass flow rate ($\text{kg}\cdot\text{h}^{-1}$)	20,000
Coolant temperature (K)	453.2
Catalyst Information	
Catalyst composition	Cu/SiO ₂
Size and shape	3 × 5 mm cylinder

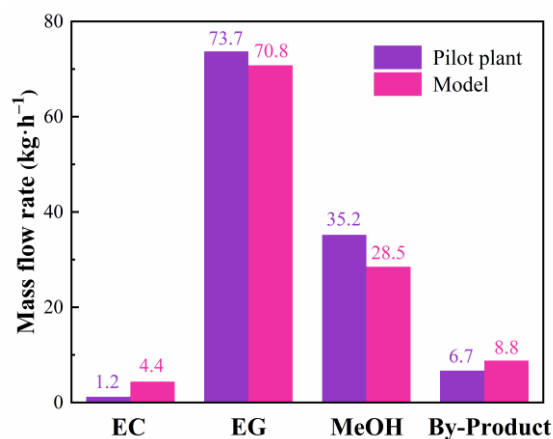


Figure 3. Comparison between pilot plant and simulation data for EC hydrogenation in the conduction oil-cooled multi-tubular reactor.

3.2. Reactor Profiles

3.2.1. Adiabatic

As the simplest form of fixed bed reactors, adiabatic reactors are often designed with multi-stage feeding in order to control the temperature rise of the catalytic bed by inter-stage cooling. For the EC hydrogenation reaction, however, the adiabatic temperature rise is estimated as only 10~20 K under typical operating conditions because of the high H_2/EC ratio, despite a considerable reaction enthalpy change (-87.3 kJ/mol). Therefore, a one-stage adiabatic reactor is considered herein in view of a facile temperature control that could be envisioned.

For the adiabatic reactor loaded with sphere catalysts (5 mm), Figure 4 shows the contours of bed temperature and partial pressures of EC and EG under three different inlet temperatures. The adiabatic reactor exhibits a plug-flow behavior with minimal radial gradients of velocity, temperature and species concentrations. In the axial (flow) direction, a mild adiabatic temperature rise of c.a. 12 K is observed, which is scarcely affected by the variation of inlet temperatures from 443 to 483 K (Figure 4a–c). With the increase of the inlet temperature, the average bed temperature increases, thus accelerating EC transformation as reflected by the decrease of average P_{EC} inside the catalyst bed. Consistently, in the front part of the catalyst bed, P_{EG} is found to increase with the inlet temperature. P_{EG} near the reactor outlet, however, is lower for higher inlet temperatures as a result of the intensified secondary EG hydrogenation reaction (R3). This side reaction has a high activation energy of 114 kJ/mol (Table S1) and is sensitive to temperature rise than the main reaction (R1). The consumption of EG in the rear part of the catalyst bed is remarkable when the local bed temperature rises to above 473 K (Figure S3), corresponding to inlet temperatures above 463 K. Therefore, maintaining a moderate bed temperature is necessary to maximize the selectivity to desired alcohol products.

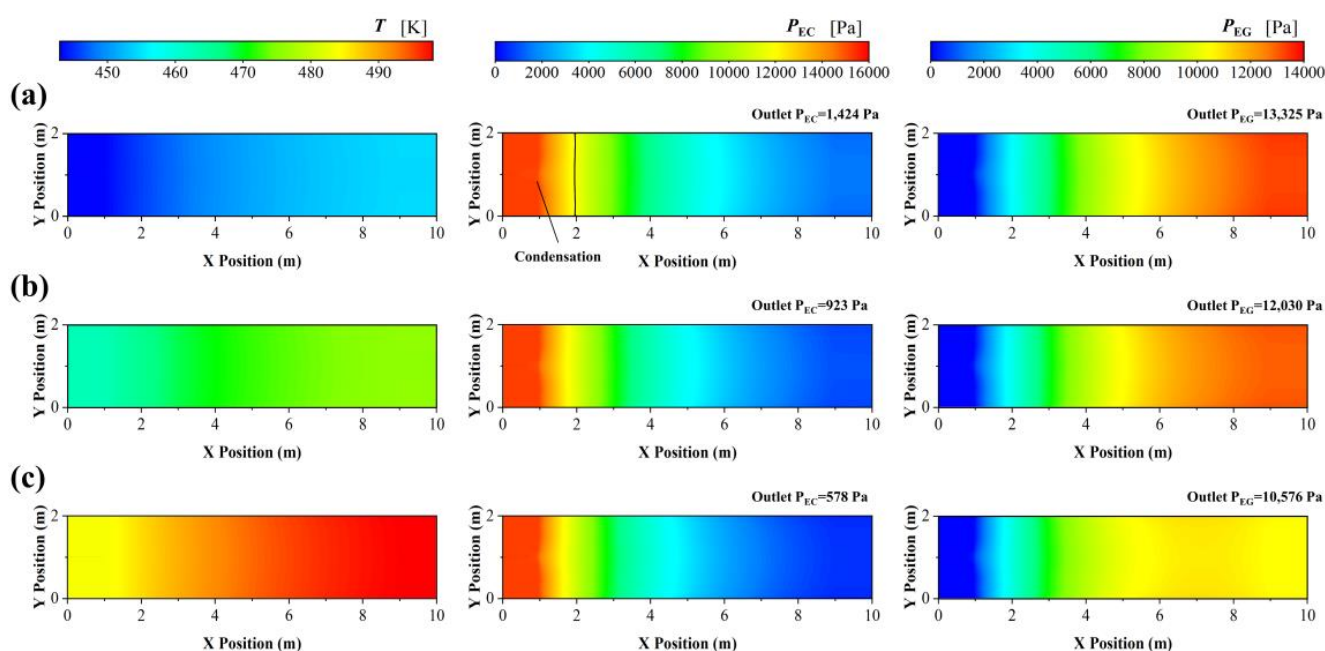


Figure 4. Contours of T , P_{EC} and P_{EG} in the adiabatic reactor with different reactant inlet temperatures of (a) 443 K, (b) 463 K and (c) 483 K under the conditions of 3 MPa, $0.3 \text{ g}_{EC} \cdot \text{g}_{cat}^{-1} \cdot \text{h}^{-1}$ and $H_2/EC = 200$.

Another necessary practical consideration for reactor operation is that EC is a high boiling-point organic liquid with a dew-point temperature of c.a. 450 K under the inlet condition (Figure S2), which overlaps with the range of operating temperatures. If EC liquefies within the catalyst bed, liquid film would cover the catalyst particle, not only blocking the active sites but also causing coking in the longer term. At the inlet temperature of 443 K, EC condensation is predicted to occur in the first c.a. 20% of the catalyst bed from

the inlet (marked by a vertical line in Figure 4a) as judged by the local partial pressure of EC. From the condensation boundary downstream to the reactor outlet, EC remains in the gas phase as a consequence of both the increasing temperature profile of the adiabatic reactor and the decreasing EC partial pressure with the reaction proceeding.

3.2.2. Boiling Water Cooling

Boiling water-cooled fixed-bed reactors often adopt a shell-and-tube structure in which multiple parallel reaction tubes are immersed in flowing boiling water in a shell. To enhance heat transfer from the tube to the coolant, a small tube diameter is chosen. Figure 5 shows the contours of bed temperature and partial pressures of EC and EG within a single reaction tube of the boiling-water cooled reactor under three different coolant temperatures. Within the first 10% of the catalyst bed, the bed temperature approaches the coolant temperature with the temperature gradients in the radial direction reducing from 20 K to zero (Figures 5a–c and S7a,c). No exotherm is observed within the entire catalyst bed in the axial direction for the three coolant temperatures. Because of the relatively low heat release from the reaction and the high convective heat transfer coefficient of boiling water, the coolant temperature rather than the reactant inlet temperature is the determining factor for the bed temperature (Figure S6a). When the coolant temperature increases, the average P_{EC} decreases with the accelerated EC hydrogenation reaction. Different from the adiabatic reactor, an upward trend is observed in P_{EG} with an increasing coolant temperature from 423 K to 463 K because EC conversion to EG is promoted whilst the EG hydrogenation side-reaction remains negligible in the temperature range. For the inlet temperature of 463 K, it is remarkable that the boiling water-cooled reactor gives rise to an EG yield $\sim 10\%$ higher than the adiabatic reactor, with only 12 K difference in the bed temperature.

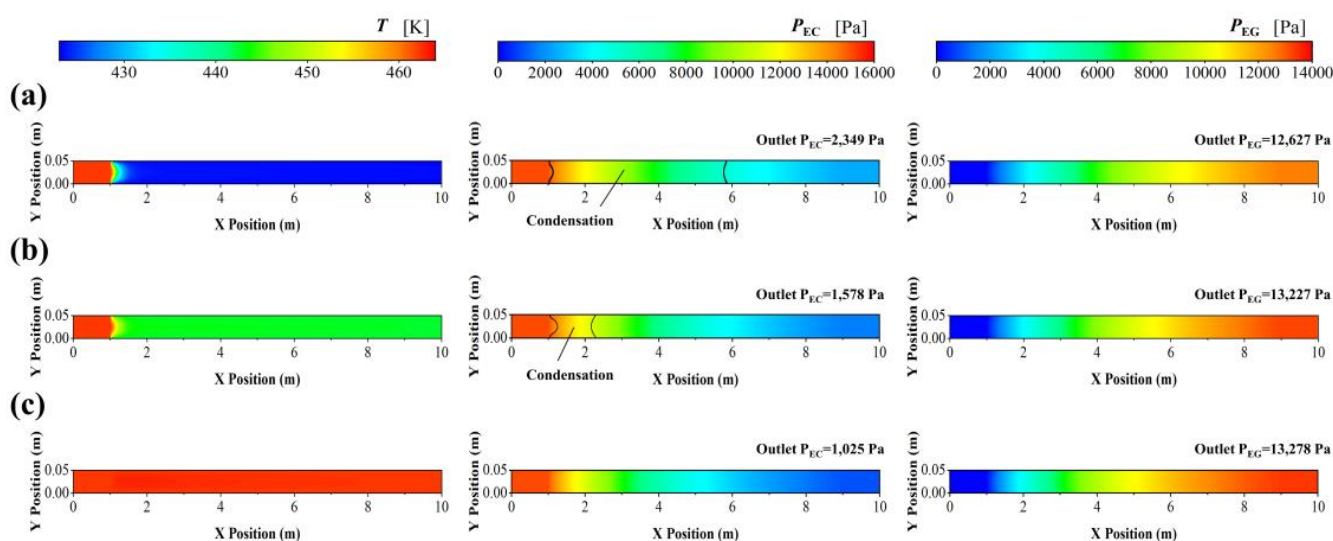


Figure 5. Contours of T , P_{EC} and P_{EG} in boiling water-cooled reactor with different coolant temperatures of (a) 423 K, (b) 443 K and (c) 463 K under the conditions of 3 MPa, $0.3 \text{ g}_{EC} \cdot \text{g}_{cat}^{-1} \cdot \text{h}^{-1}$, $\text{H}_2/\text{EC} = 200$ and reactant inlet temperature of 463 K.

The lower bed temperatures relative to the adiabatic reactor increase the risk of EC condensation. Figure 5a,b illustrate that the condensation zones are more extended in the near-wall region than around the reactor centerline. Due to an oscillatory increasing bed porosity towards the reactor wall (Table S5), the EC flowrate increase towards the wall (Figures S4 and S5), contributing to higher local partial pressures of EC. Such a behavior is prominent for the multi-tubular heat-exchange reactors with high tube-to-particle diameter ratios and thus considerable channeling flows near the wall.

3.2.3. Conduction Oil Cooling

In the pilot plant reactor, conduction oil is selected as the coolant in consideration of easiness of control and its satisfactory performance of heat removal. The heat transfer coefficients of conduction oils are significantly lower than the boiling water and depend on geometrical and operational parameters such as the oil flow rates, the distance between adjacent baffle plates, the type of baffle, etc. The specific relationships are given in the Supporting Information (Section S3.2). In general, conduction oil is not as effective as boiling water in controlling the reactor temperature, especially under low oil flow rates. Taking 25% open baffle, 1 m distance between adjacent baffle plates and the $200,000 \text{ kg}\cdot\text{h}^{-1}$ mass flow rate as the reference case, the resulting heat transfer coefficient is calculated to be $619 \text{ W}\cdot\text{m}^{-2}\cdot\text{K}^{-1}$. These values will be used in the following study.

Figure 6 shows that the bed temperature drops quickly close to the inlet of the oil-cooled reactor as a consequence of the low inlet temperature of the conduction oil. Then, with the oil being heated up continuously by the exothermic reaction, the bed temperature gradually rises towards the reactor outlet (Figure 6a–c and Figure S7a). The radial temperature gradient in the catalyst bed reduces from 9 K at the inlet to zero after 10% of the catalyst bed. Distinct from that of the boiling water-cooled reactor, the bed temperature of the oil-cooled reactor is also affected by the inlet temperature of reactants: both the increase of reactant inlet temperature and the coolant inlet temperature decrease the EG selectivity (Figure S6b). Different also from both the adiabatic and the boiling water-cooled reactors is that P_{EG} increases slightly with the bed temperature for oil inlet temperatures below 463 K, but decreases slightly with the bed temperature when the oil inlet temperature exceeds 463 K. The outlet flow rates of EG are the highest among the studied reactor types for reactant inlet temperatures between 423 and 463 K thanks to the moderate temperature profile, which balances between promoting EC conversion and preventing secondary EG hydrogenation. Meanwhile, the predicted condensation region of EC is significantly smaller than that of the boiling-water cooled reactor, and the condensation only appears under the lowest coolant temperature of 423 K.

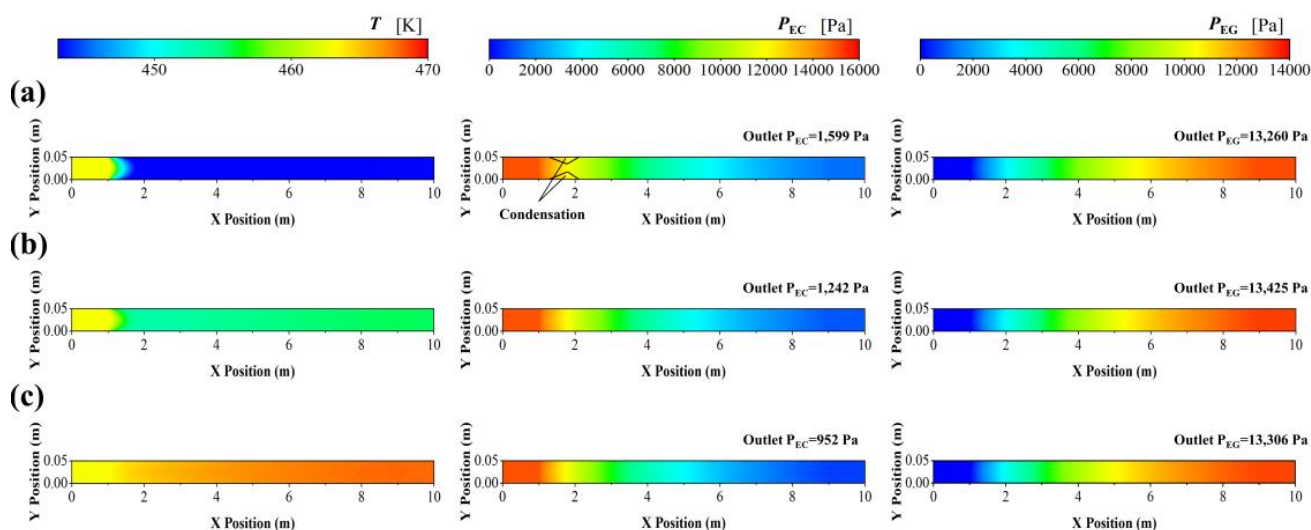


Figure 6. Contours of T , P_{EC} and P_{EG} in oil-cooled reactor with different coolant temperatures of (a) 423 K, (b) 443 K and (c) 463 K under the conditions of 3 MPa, $0.3 \text{ g}_{\text{EC}}\cdot\text{g}_{\text{cat}}^{-1}\cdot\text{h}^{-1}$, $\text{H}_2/\text{EC} = 200$ and reactant inlet temperature of 463 K.

3.3. Effects of Key Operating Variables

To elaborate the reactor's operation behaviors, the effects of major operation variables on the reactor performance are further depicted. Five operation variables are studied, including the inlet temperature T_{in} , the coolant temperature T_{c} , the operating pressure P_{op} , the

space velocity SV , and the inlet H_2/EC . The chosen performance metrics are EC conversion X_{EC} , EG selectivity S_{EG} , MeOH selectivity S_{MeOH} and total alcohols selectivity $S_{Alcohol}$.

3.3.1. Temperature

For all reactor types, Figure 7 shows that X_{EC} and S_{MeOH} increase while S_{EG} and $S_{Alcohol}$ decrease with the increase of inlet temperature. At higher temperatures, the faster reaction results in a greater amount of EC being converted (X_{EC} rises). Given that the activation energies of Reaction 1, 2 and 3 (R1)–(R3) are 30.1, 28.1 and 113.8 $\text{kJ}\cdot\text{mol}^{-1}$, respectively (Table S1), higher temperatures promote hydrogenation of EG to by-products (S_{EG} decreases) but inhibits EC conversion to CO instead of MeOH (S_{MeOH} increases). Comparison among different reactor types (Figure 7a–d) show slight differences in the EC conversion. X_{EC} of the adiabatic reactor is higher than that of the other two types of reactor owing to its high average temperature of the catalyst bed. X_{EC} of the boiling water-cooled reactor is the lowest among the three types of reactor, but the difference from that of the oil-cooled reactor diminishes as the coolant temperature is raised above 453 K. Since the reactant inlet temperature also affects the performance of the oil-cooled reactor, Figure 7d additionally illustrates the effect of reactant inlet temperature on X_{EC} , S_{EG} , S_{MeOH} and $S_{Alcohol}$. The variations in the reactant inlet temperature and the oil temperature exhibit similar influences on the reactor performance.

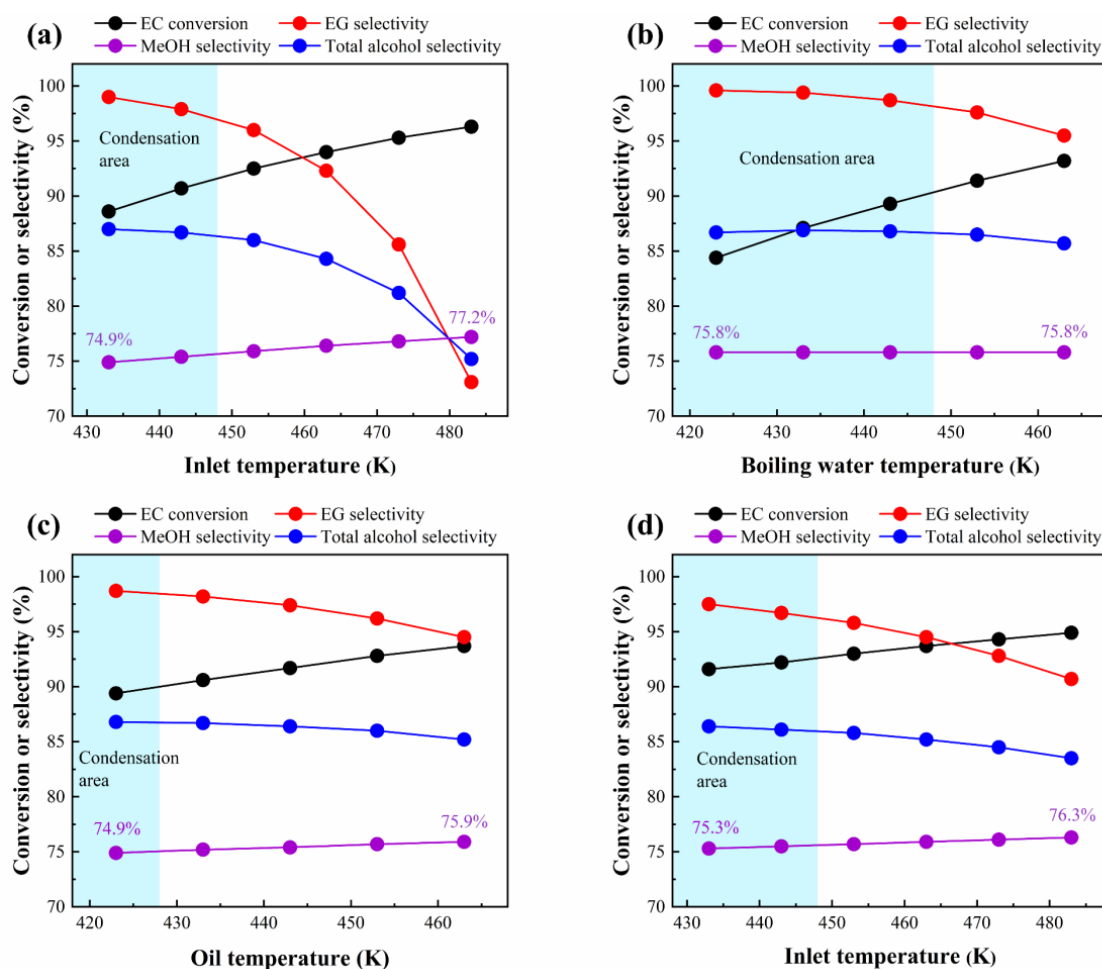


Figure 7. Reactor performance under different reactant/coolant inlet temperatures: (a) adiabatic reactor with $T_{in} = 433\text{--}483$ K, (b) boiling water-cooled reactor with $T_{in} = 463$ K and $T_c = 423\text{--}463$ K, (c) conduction oil-cooled reactor with $T_{in} = 463$ K and $T_c = 423\text{--}463$ K, (d) conduction oil-cooled reactor with $T_c = 463$ K and $T_{in} = 433\text{--}483$ K. Operating conditions: 3 MPa, $0.3 \text{ g}_{EC}\cdot\text{gcat}^{-1}\cdot\text{h}^{-1}$, $H_2/EC = 200$.

EC condensation occurs in the boiling water-cooled reactor when the boiling water temperature is 448 K (Figure 7b). This critical temperature is consistent with the reactant inlet temperature leading to condensation in the adiabatic and oil-cooled reactors (Figure 7a,d) because their inlet regions are the most prone to condensation. For the oil-cooled reactor, moderate heat removal by the conduction oil combined with its relatively low heat capacity yields a bed temperature higher than the initial oil temperature. Therefore, condensation with a fixed reactant inlet temperature of 463 K does not occur until the oil temperature is lowered to 428 K (Figure 7c).

3.3.2. H₂/EC

In this work, a higher H₂/EC means lower EC partial pressures under almost the same H₂ partial pressure (the variation in the H₂ partial pressure is negligible for H₂/EC > 80). As shown in Figure 8a–c, higher H₂/EC inhibits EC conversion because the EC consumption reactions (R1 and R2) are positive-order with respect to EC. For the adiabatic reactor, the MeOH selectivity increases slightly with H₂/EC (Figure 8a). The reason is that S_{MeOH} is related to parallel reactions R1 and R2, which are 0.65-order and 1-order with respect to EC, respectively. The lower the EC partial pressure, the lower the relative rate of Reaction 1 to Reaction 2, and therefore the higher the MeOH selectivity. The EG selectivity increases more significantly with H₂/EC, because enhanced axial convective heat transfer by the gas mixture under high H₂/EC alleviates the adiabatic rise of bed temperature, which favors EG selectivity. For the boiling water-cooled reactor, the variation of S_{MeOH} with H₂/EC in Figure 8b resembles that for the adiabatic reactor. However, S_{EG} and $S_{Alcohol}$ of the water-cooled reactor only increase by 1% and 3%, respectively, for H₂/EC from 80 to 200, because the catalyst bed is close to isothermal. In Figure 8c, almost identical behavior is observed for the oil-cooled reactor as the boiling water-cooled reactor, except that X_{EC} of the latter is slightly higher for H₂/EC > 160, and that S_{EG} and $S_{Alcohol}$ of the latter is slightly lower for H₂/EC < 120. EC condensation happens when inlet H₂/EC is smaller than 120 regardless of the type of the reactor, provided that EC most likely liquefies at the reactor inlet when its partial pressure is the highest.

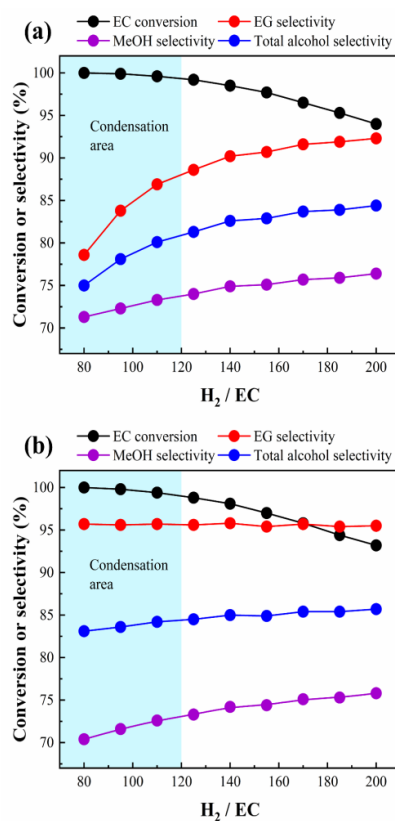


Figure 8. Cont.

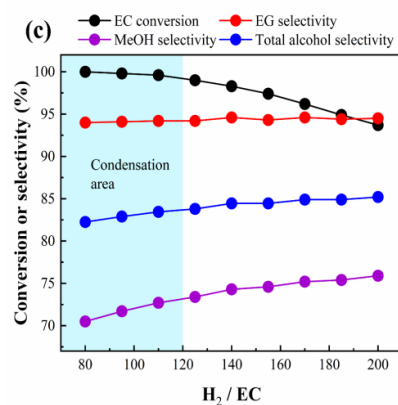


Figure 8. Reactor performance under different H_2/EC : (a) adiabatic reactor, (b) boiling water-cooled reactor, (c) conduction oil-cooled reactor. Operating conditions: reactant and coolant inlet temperatures 463 K, 3 MPa, $0.3 \text{ g}_{EC} \cdot \text{g}_{cat}^{-1} \cdot \text{h}^{-1}$, 80–200 H_2/EC .

3.3.3. Pressure and Space Velocity

Pressure and space velocity have a great impact on the catalytic reaction but a minor influence on the transport characteristics. The influence of pressure and space velocity on the reactor performance is exemplified by the case of the boiling water-cooled reactor in view of the consistent behaviors among the different types of reactors. Figure 9a shows that the increase of operating pressures accelerates EC hydrogenation as the partial pressure of EC is increased (R1) and (R3). Meanwhile, since R1 and R2 are boosted at higher pressure while remaining unaffected, an increase in EG selectivity is observed. The MeOH selectivity is determined by the relative rates between R1 and R2. With a higher total pressure and EC partial pressure, the rate of R1 increases less than that of R2 (EC orders 0.65 and 1), resulting in lower MeOH selectivity. Although a higher operating pressure favors both EC conversion and the selectivity of EG—the more value-added product—it may also lead to EC condensation when exceeding 4.8 MPa. The optimal operating pressure is around 3 MPa when all performance metrics achieves a reasonable trade-off.

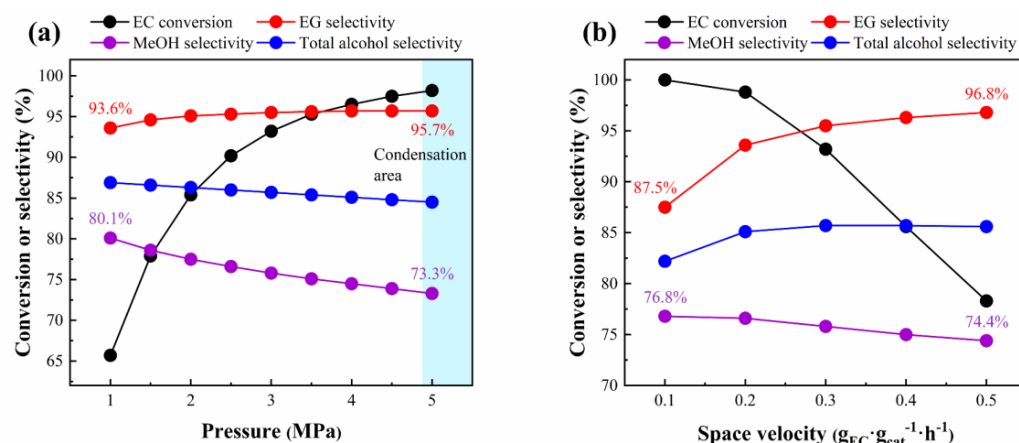


Figure 9. Reactor performance of the boiling water-cooled reactor under the conditions of (a) 1–5 MPa, $0.3 \text{ g}_{EC} \cdot \text{g}_{cat}^{-1} \cdot \text{h}^{-1}$, (b) 3 MPa, $0.1\text{--}0.5 \text{ g}_{EC} \cdot \text{g}_{cat}^{-1} \cdot \text{h}^{-1}$ ($T_{in} = 463 \text{ K}$, $T_c = 463 \text{ K}$ and $H_2/EC = 200$).

Figure 9b depicts the influence of space velocity on the reactor performance. Lower space velocity is beneficial for both X_{EC} and S_{MeOH} . To ensure a conversion over 90%, the space velocity should be maintained below $0.3 \text{ g}_{EC} \cdot \text{g}_{cat}^{-1} \cdot \text{h}^{-1}$. The slightly higher MeOH selectivity at low SV and high X_{EC} originates from the fact that the main reaction R1 has a smaller reaction order of EC than the parallel side-reaction R2 (i.e., R1 decays slower at high EC conversion than R2). In contrast to MeOH, the EG selectivity is boosted at high SV when the secondary EG hydrogenation reaction proceeds inadequately. Since

high space velocity results in too large bed pressure drop (Figure S5b), a space velocity of around $0.3 \text{ g}_{\text{EC}} \cdot \text{g}_{\text{cat}}^{-1} \cdot \text{h}^{-1}$ is deemed feasible with balanced operational cost and reaction performance.

The specific effects of key operating variables T , P_{op} , SV and H_2/EC on the reactor performance are summarized in the Table S7.

3.4. Operation Windows

Informed by the preceding illustrations, the different types of reactors response differently to variations of operating parameters. The major variables that affect the reactor performance and could be frequently changed in industrial practice include the inlet temperature of reactants and coolant (T), the operating pressure (P_{op}), and space velocity (SV). Therefore, the T , P_{op} and SV values required to reach certain X_{EC} , S_{EG} and S_{Alcohol} are further calculated for the different types of reactors to shed light on their respective operating windows.

Figure 10 shows the demanded temperature and operating pressure for X_{EC} , S_{EG} and S_{Alcohol} to reach 90/95/98%, respectively. In brief, the contour lines for $X_{\text{EC}} = 90\%$ and 98% indicate that higher temperatures are required should the EC conversion be kept constant at decreasing operating pressures. The contour lines for $S_{\text{EG}} = 90\%$ and 95% indicate that the operating pressure has negligible effects on S_{EG} , which only decreases with the increase of temperature. The 85% S_{Alcohol} contour line shows a downward trend with temperature for $P_{\text{op}} > 3.5 \text{ MPa}$. This is because higher pressures decrease S_{MeOH} with S_{EG} unaffected; thus, lower temperatures are demanded to compensate for the decrease in S_{Alcohol} . Additionally, EC condensation restrains the allowable scope of the operation variables; the condensation regimes for the different types of reactors are marked in cyan in Figure 10. As P_{op} increases, the dewpoint temperature of EC rises, thus enlarging the condensation regime. In Figure 10b,c, EC condensation is unavoidable regardless of the coolant temperature for $P_{\text{op}} > 4.9 \text{ MPa}$ because the reactants condensate at the reactor inlet with the given inlet temperature of 463 K.

For all types of reactors under investigation, the contour lines divide the reactor's operating window (T and P_{op}) into different regimes with distinct reactor performance. For instance, the red, triangular zone in Figure 10a denotes the T_{in} and P_{op} window for the adiabatic reactor to achieve $X_{\text{EC}} > 90\%$ and $S_{\text{EG}} > 95\%$ under the SV of $0.3 \text{ g}_{\text{EC}} \cdot \text{g}_{\text{cat}}^{-1} \cdot \text{h}^{-1}$ and inlet H_2/EC of 200. Figure 10a also indicates that the adiabatic reactor is not operable if $X_{\text{EC}} > 98\%$ and $S_{\text{EG}} > 95\%$ are desired, as the corresponding regimes would overlap inside the EC condensation regime with pressures over 5 MPa and inlet temperature below 450 K. It can be concluded that the adiabatic reactor is difficult to operate under pressures $> 4 \text{ MPa}$ owing to a very narrow range of feasible inlet temperatures for adequate product yields. In contrast to the adiabatic reactor, Figure 10b–d demonstrate that the boiling water and conduction oil-cooled reactors exhibit wider operating windows of the inlet/coolant temperatures under higher pressures. The reason is twofold: First, heat removal uplifts the contour lines of S_{EG} in the case of boiling water cooling and in the case of oil cooling with varying inlet temperatures (Figure 10b,d). Second, the ascending temperature profile along the oil-cooled reactor drastically lowers the EC condensation line on the oil inlet temperature-reactor pressure diagram (Figure 10c). The reactors with heat exchange would allow $X_{\text{EC}} > 98\%$ and $S_{\text{EG}} > 95\%$ with the demanded T_{c} and P_{op} being 463–465 K and 4.8–4.9 MPa for the boiling water-cooled reactor (green zone, Figure 10b), and 458–461 K and 4.8–4.9 MPa for $T_{\text{in}} = 463 \text{ K}$, or 466–474 K and 4.8–5.0 MPa for $T_{\text{c}} = 453 \text{ K}$, respectively, for the conduction oil-cooled reactor (Figure 10c,d). In all, the conduction oil-cooled reactor demonstrates the best operability in terms of allowable reactant/coolant inlet temperatures, especially under lower pressures.

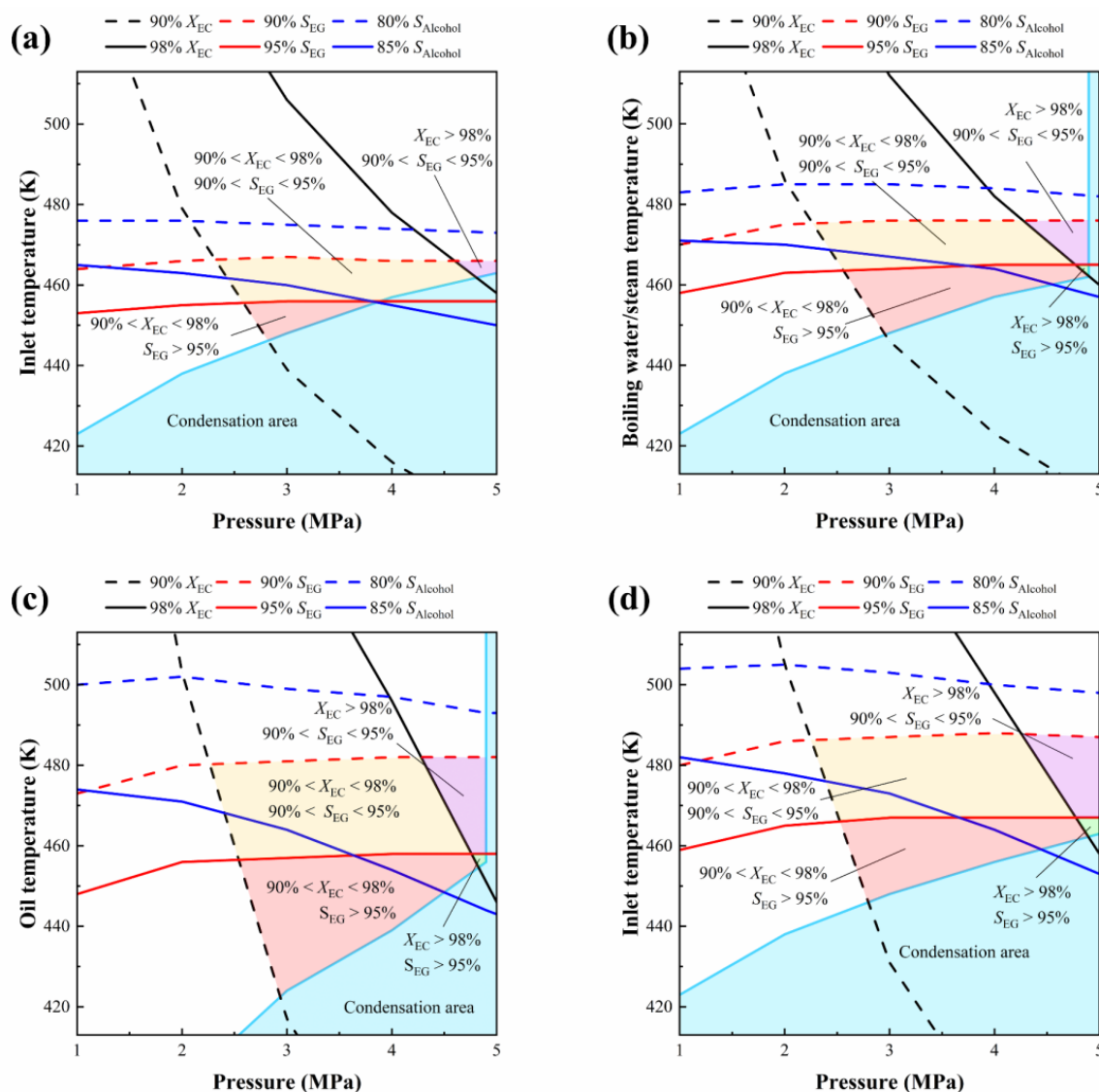


Figure 10. Operation windows of reactors for demanded $T_{in}/T_c - P_{op}$ parameters on outlet EC conversion, EG selectivity and total alcohol selectivity under $SV = 0.3 \text{ g}_{EC} \cdot \text{g}_{cat}^{-1} \cdot \text{h}^{-1}$ and $H_2/EC = 200$. Reactor type: (a) adiabatic, (b) boiling water-cooled, (c) oil-cooled, $T_{in} = 463 \text{ K}$, (d) oil-cooled, $T_c = 453 \text{ K}$.

As the production capacity of reactors might be varied during industrial operation, we further investigated the reactors' operating windows with respect to various T_{in}/T_c and SV in with P_{op} and H_2/EC set to 3 MPa and 200, respectively. Figure 11 shows that increasing temperature with the space velocity is required in order to maintain certain EC conversions, and in contrast, the maximum temperature limits to keep the EG selectivity and total alcohols selectivity above thresholds are uplifted under a higher SV . An exception is found for the oil-cooled reactor with varying inlet temperatures, where the maximum inlet temperature allowable for 85% total alcohols selectivity decreases again with the increase of space velocity at above c.a. $0.4 \text{ g}_{EC} \cdot \text{g}_{cat}^{-1} \cdot \text{h}^{-1}$. The EC condensation regime remains invariant with the space velocity for the adiabatic and boiling water-cooled reactor, as well as for the oil-cooled reactor with varying reactant inlet temperatures. In these cases, whether EC condensates in the catalyst bed is determined by the inlet conditions. For the oil-cooled reactor with varying oil inlet temperatures, the EC condensation regime shifts to lower temperatures with increasing space velocity, under which conditions the initial sink of bed temperature due to cooling is less prominent.

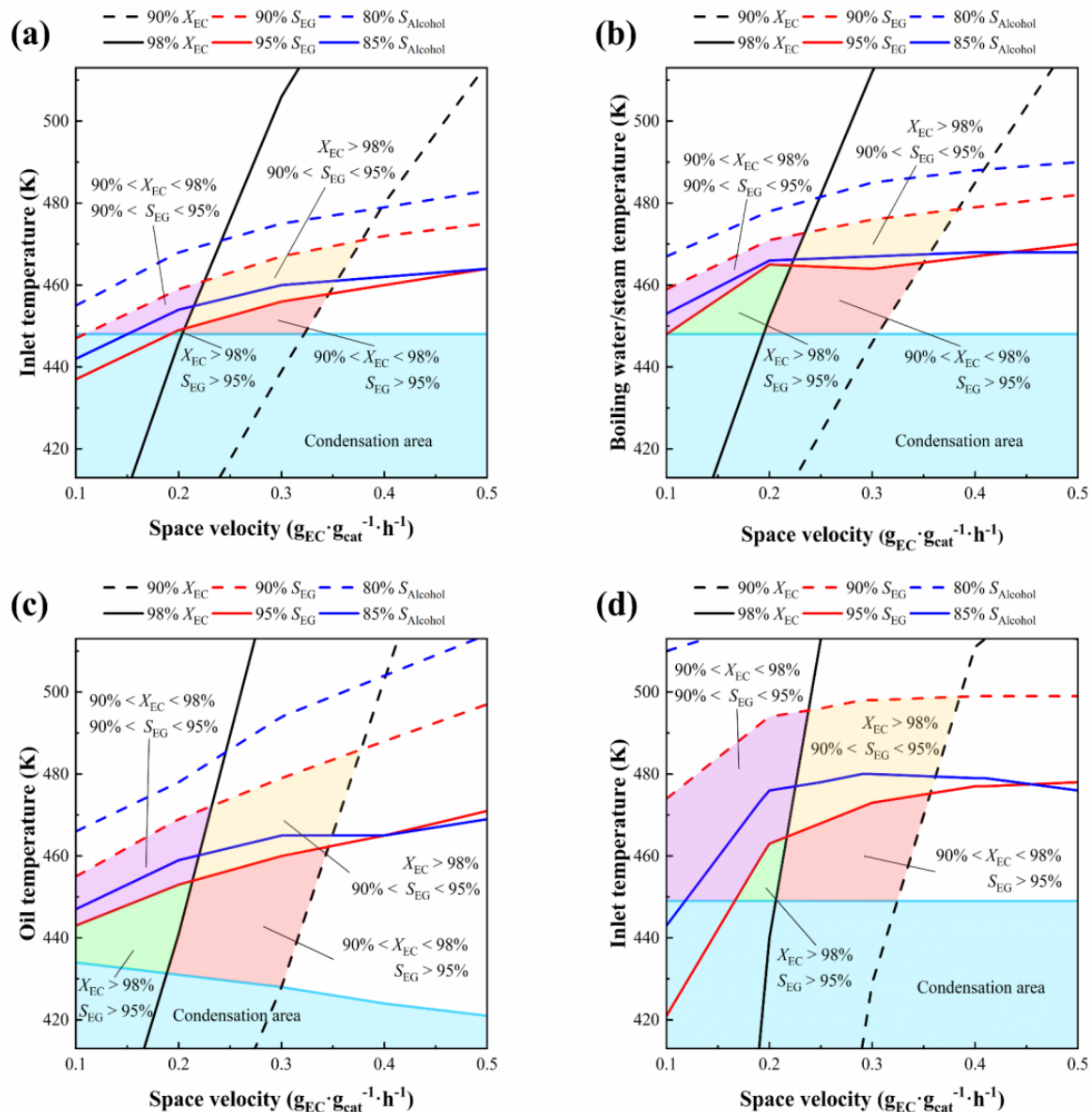


Figure 11. Operation windows of reactors for demanded T_{in}/T_c -SV parameters on outlet EC conversion, EG selectivity and total alcohol selectivity under 3 MPa and 200 H_2/EC . Reactor type: (a) adiabatic, (b) boiling water-cooled, (c) oil-cooled, $T_{in} = 463$ K, (d) oil-cooled, $T_c = 453$ K.

A very small operation window for $X_{EC} > 98\%$ and $S_{EG} > 95\%$ (green zone; T_{in} of 448–449 K, SV of 0.19–0.20 $g_{EC} \cdot g_{cat}^{-1} \cdot h^{-1}$) is shown for the adiabatic reactor in Figure 11a. However, common fluctuations in industry makes it difficult to keep T_{in} and SV static in the range. For the boiling water-cooled reactor, the corresponding ranges of T_c and SV are c.a. 448–463 K and 0.10–0.22 $g_{EC} \cdot g_{cat}^{-1} \cdot h^{-1}$, respectively, while for the conduction oil-cooled reactor with varying oil inlet temperatures, the ranges of T_c and SV are c.a. 432–454 K and 0.10–0.21 $g_{EC} \cdot g_{cat}^{-1} \cdot h^{-1}$. As in Figure 11b–d, the larger T_c -SV window of the boiling water-cooled reactor benefits from an isothermal temperature profile that avoids deteriorating S_{EG} at higher water temperatures, while that of the conduction oil-cooled reactor from a wide non-condensable regime. To sum up, the conduction oil-cooled reactor has the greatest allowable scope of space velocity for a wide range of reactant/coolant inlet temperatures.

4. Conclusions

In this work, multiscale reactor models for heterogeneous EC hydrogenation to co-produce MeOH and EG in industrial-type adiabatic, water-cooled and oil-cooled tubular fixed-bed reactors are established and validated with bench-scale and pilot plant data. The main and side reactions occurring during the heterogeneous EC hydrogenation over Cu-based catalysts are described by a power-law engineering kinetics model involving three independent reactions.

EC hydrogenation under typical operating conditions in the adiabatic reactor renders a mild temperature rise of c.a. 12 K. However, bed temperatures above 473 K would significantly reduce the selectivity to the primary product EG due to its secondary hydrogenation, which is more temperature-sensitive than the main EC hydrogenation reaction. If the inlet temperature is lower than 453 K, however, EC condensation might happen and deactivate the catalyst, especially under low H_2/EC and high operating pressures. The boiling water-cooled reactor behaves close to isothermally regardless of the reactant inlet temperature, with temperature gradients only existing in the first 10% of the catalyst bed, which is beneficial for the improving the yield of EG. The conduction oil-cooled reactor shows a minimum bed temperature near the bed entrance as the cold oil gets constantly heated up towards the bed outlet. Such a U-shape temperature profile allows a relatively wide scope of both the reactant inlet temperature and the oil inlet temperature with adequate reactor performance.

Model-based operational analysis of the three different types of reactors further suggests that the application of the adiabatic reactor in EC hydrogenation is restrained by a very narrow operating window of the inlet temperature, especially under higher pressures and space velocities, if practical EC conversion and alcohols selectivity are to be acquired within the non-condensable regime of EC. The boiling water-cooled reactor exhibits no restraint on the reactant inlet temperature and a relatively wide window of the coolant temperature under different pressures and space velocities. The conduction oil-cooled reactor has a sufficiently wide window of the reactant inlet temperature and a larger operating window of the coolant temperature than the water-cooled reactor. This enables reactor operation under higher pressures and space velocities, thus providing a greater production flexibility. Understanding of these operational characteristics of representative industrial-type reactors for EC hydrogenation not only reveals the key in reactor design, but will also pave the way to further process optimization.

Supplementary Materials: The following supporting information can be downloaded at: <https://www.mdpi.com/article/10.3390/pr10040688/s1>, Figure S1: Model and experiment values deviation of EC hydrogenation reaction; Figure S2: EC condensation zone under the condition of $T = 410\text{--}530\text{ K}$, $P_{op} = 1\text{--}5\text{ MPa}$ and $H_2/EC = 40\text{--}200$; Figure S3: Contours of P_{EG} in different heat-exchange-type reactors: (a) (d) (g) adiabatic, (b) (e) (h) boiling water-cooled, (c) (f) (i) oil-cooled, under the conditions of 3 MPa, $0.3\text{ g}_{EC}\cdot\text{g}_{cat}^{-1}\cdot\text{h}^{-1}$, 200 H_2/EC and inlet/coolant temperatures of (a) (d) (g) inlet temperatures 443, 463, 483 K, (b)/(c) (e)/(f) (h)/(i) inlet temperature 463 K, coolant temperatures 423, 443, 463 K; Figure S4: Contours of u_0 in different heat exchange type reactor: (a) adiabatic (b) boiling water-cooled (c) oil-cooled under the conditions of 3 MPa, $0.3\text{ g}_{EC}\cdot\text{g}_{cat}^{-1}\cdot\text{h}^{-1}$, 200 H_2/EC , 463 K inlet temperature and 463 K coolant temperature; Figure S5: The influence of SV on (a) superficial velocity and (b) bed pressure drop, in boiling water-cooled reactor under the conditions of 3 MPa, $0.3\text{ g}_{EC}\cdot\text{g}_{cat}^{-1}\cdot\text{h}^{-1}$ and 200 H_2/EC ; Figure S6: The influence of reactant/coolant inlet temperatures on S_{EG} under the conditions of 3 MPa, $0.3\text{ g}_{EC}\cdot\text{g}_{cat}^{-1}\cdot\text{h}^{-1}$ and 200 H_2/EC : (a) boiling water-cooled, (b) conduction oil-cooled reactor; Figure S7: Under the conditions of 3 MPa, $0.3\text{ g}_{EC}\cdot\text{g}_{cat}^{-1}\cdot\text{h}^{-1}$ and 200 H_2/EC , (a) bed and coolant temperatures in the axial direction; bed temperatures in the radial direction: (b) adiabatic, $T_{in} = 443\text{ K}$, (c) boiling water-cooled, $T_{in} = 463\text{ K}$ and $T_c = 443\text{ K}$ (d) conduction oil-cooled reactors, $T_{in} = 463\text{ K}$ and $T_c = 423\text{ K}$; Table S1: Intrinsic kinetic parameters; Table S2: Specific heat capacity; Table S3: Thermal conductivity; Table S4: Viscosity; Table S5: Bed voidage; Table S6: Influence of catalyst sizes and shapes on reactor performance; Table S7: Effect of key operating variables on X_{EC} , S_{EG} , S_{MeOH} . Refs. [62,64,65] are cited in supplementary materials.

Author Contributions: Conceptualization, C.C.; Funding acquisition, Y.W., J.L. and J.X.; Investigation, H.H., C.C. and Y.Y.; Methodology, C.C. and Y.W.; Project administration, Y.W., J.L. and J.X.; Supervision, C.C. and J.X.; Writing—original draft preparation, H.H.; Writing—review and editing, C.C., Y.W., J.L. and J.X. All authors have read and agreed to the published version of the manuscript.

Funding: This research was funded by the National Natural Science Fund for Distinguished Young Scholars (61725301), International (Regional) Cooperation and Exchange Project (61720106008), National Natural Science Foundation of China (21878080, 61973124), and the Dean/Opening Project of Guangxi Key Laboratory of Petrochemical Resource Processing and Process Intensification Technology.

Data Availability Statement: Data available on request due to restrictions e.g., privacy or ethical.

Conflicts of Interest: The authors declare no conflict of interest.

Notations

a	Surface area of particles per unit volume (m^{-1})
$c_{p,f}$	Specific heat capacity of fluid ($\text{J}\cdot\text{kg}^{-1}\cdot\text{K}^{-1}$)
$c_{p,oil}$	Specific heat capacity of conduction oil ($\text{J}\cdot\text{kg}^{-1}\cdot\text{K}^{-1}$)
C_2	Inertial loss coefficient (m^{-1})
$C_{EC,center}$	Concentration of EC in the center of catalyst ($\text{kmol}\cdot\text{m}^{-3}$)
$C_{EC,gas}$	Concentration of EC in the gas phase ($\text{kmol}\cdot\text{m}^{-3}$)
$C_{EC,s}$	Concentration of EC on the surface of catalyst ($\text{kmol}\cdot\text{m}^{-3}$)
d_p	Diameter of sphere (m)
d_p^a	Diameter of sphere with equal specific surface area (m)
d_p^s	Diameter of sphere with equal surface area (m)
d_p^v	Diameter of sphere with equal volume (m)
D	Bed or tube diameter (m)
$D_{e,ax}$	Effective axial diffusion coefficient ($\text{m}^2\cdot\text{s}^{-1}$)
$D_{e,r}$	Effective radial diffusion coefficient ($\text{m}^2\cdot\text{s}^{-1}$)
$D_{eff,EC}$	Effective diffusion coefficient of EC in the catalyst particle ($\text{m}^2\cdot\text{s}^{-1}$)
$D_{EC,m}$	Molecular diffusivity of EC ($\text{m}^2\cdot\text{s}^{-1}$)
$D_{T,i}$	Thermal diffusion coefficient ($\text{kg}\cdot\text{m}^{-1}\cdot\text{s}^{-1}$)
E_f	Total fluid energy ($\text{m}^2\cdot\text{s}^{-2}$)
E_s	Total solid energy ($\text{m}^2\cdot\text{s}^{-2}$)
h_j^0	Enthalpy of formation of species j ($\text{J}\cdot\text{kmol}^{-1}$)
H_2/EC	Molar ratio of EC to H_2
J_i	Diffusion flux of species i vector ($\text{kg}\cdot\text{m}^{-2}\cdot\text{s}^{-1}$)
k	Turbulence kinetic energy
$k_{e,ax}$	Effective axial thermal conductivity ($\text{W}\cdot\text{m}^{-1}\cdot\text{K}^{-1}$)
$k_{e,r}$	Effective radial thermal conductivity ($\text{W}\cdot\text{m}^{-1}\cdot\text{K}^{-1}$)
k_f	Thermal conductivity of fluid ($\text{W}\cdot\text{m}^{-1}\cdot\text{K}^{-1}$)
k_g	Gas-solid mass transfer coefficient ($\text{m}\cdot\text{s}^{-1}$)
k_s	Thermal conductivity of catalyst particle ($\text{W}\cdot\text{m}^{-1}\cdot\text{K}^{-1}$)
k_v	Pre-exponential factor
L	Bed length (m)
$\dot{m}_{EC,in}$	EC inlet mass flow ($\text{kg}\cdot\text{h}^{-1}$)
$\dot{m}_{EC,out}$	EC outlet mass flow ($\text{kg}\cdot\text{h}^{-1}$)
$\dot{m}_{EG,out}$	EG outlet mass flow ($\text{kg}\cdot\text{h}^{-1}$)
$\dot{m}_{MeOH,out}$	MeOH outlet mass flow ($\text{kg}\cdot\text{h}^{-1}$)
\dot{m}_{oil}	Conduction oil mass flow ($\text{kg}\cdot\text{h}^{-1}$)
M_w	Molecular weight ($\text{kg}\cdot\text{kmol}^{-1}$)
n	Reaction order
Nu	Nusselt number
p	Static pressure (Pa)
P_{EC}	EC partial pressure (Pa)
P_{EG}	EG partial pressure (Pa)

P_{op}	Operating pressure (MPa)
Pe_h^0	Fluid Peclet number for heat transfer
$Pe_{h,ax}$	Peclet number for axial heat conduction
$Pe_{h,r}^\infty$	Peclet radial heat transfer for fully developed turbulence flow
$Pe_{m,ax}$	Peclet number for axial mass dispersion
$Pe_{m,r}$	Peclet number for radial mass dispersion
Pr	Prandtl number
Q_{oil}	Heat flux to oil (W)
$Q_{reaction}$	Reaction heat (W)
r_{chem}	Intrinsic reaction rate ($\text{kmol}\cdot\text{m}^{-3}\cdot\text{s}^{-1}$)
r_{obs}	Effective reaction rate ($\text{kmol}\cdot\text{m}^{-3}\cdot\text{s}^{-1}$)
R	Ratio of tube diameter to catalyst's volume-equivalent diameter
$R_{EC,s}$	Effective consumption rate of EC at the particle surface ($\text{kmol}\cdot\text{m}^{-3}\cdot\text{s}^{-1}$)
R_j	Volumetric rate of creation of species j ($\text{kmol}\cdot\text{m}^{-3}\cdot\text{s}^{-1}$)
Re	Reynolds number based on particle diameter
$S_{Alcohol}$	Total alcohol selectivity
S_{cat}	Surface area of catalyst particle (m^2)
S_{EG}	EG selectivity
S_f^h	Energy source term ($\text{W}\cdot\text{m}^{-3}$)
S_i	Mass source term ($\text{kg}\cdot\text{m}^{-3}\cdot\text{s}^{-1}$)
S_{MeOH}	MeOH selectivity
S_{wall}	Surface area of wall (m^2)
S_ϕ	Momentum source term ($\text{kg}\cdot\text{m}^{-2}\cdot\text{s}^{-2}$)
Sc	Schmidt number
Sh	Sherwood number
SV	Space velocity ($\text{g}_{EC}\cdot\text{g}_{cat}^{-1}\cdot\text{h}^{-1}$)
t	Time (s) or adjacent baffle plate space (m)
T	Temperature (K)
T_b	Boiling point of pressurized water (K)
T_c	Coolant temperature (K)
T_{in}	Reactant inlet temperature (K)
T_{oil}	Conduction oil temperature (K)
T_s	Catalyst surface temperature (K)
T_w	Wall temperature (K)
u_0	Superficial velocity ($\text{m}\cdot\text{s}^{-1}$)
v	Fluid flow velocity vector ($\text{m}\cdot\text{s}^{-1}$)
v_{cat}	Volume of catalyst particle (m^3)
x	X position along the bed axial direction (m)
X_{EC}	EC conversion
X_i	Mass fraction of species i
Y_i	Mole fraction of species i
<i>Greek letters</i>	
α_f	Gas-solid heat transfer coefficient ($\text{W}\cdot\text{m}^{-2}\cdot\text{K}^{-1}$)
$\Delta_r H$	Enthalpy of reaction ($\text{J}\cdot\text{kmol}^{-1}$)
ΔP	Bed pressure drop (Pa)
ΔT_{ex}	Temperature difference between catalyst surface and gas phase (K)
ΔT_{in}	Temperature difference between catalyst surface and center (K)
ϵ_b	Bed voidage
ϵ_{cat}	Internal porosity of catalyst particle
η_{EC}	Effectiveness factor for EC internal mass transfer
$\lambda_{eff,cat}$	Effective thermal conductivity of catalyst particle ($\text{W}\cdot\text{m}^{-1}\cdot\text{K}^{-1}$)
μ	Fluid viscosity (Pa·s)
ρ_f	Fluid density ($\text{kg}\cdot\text{m}^{-3}$)
τ	Stress tensor (Pa)
$\phi_{gen,EC}$	Generalized Thiele modulus of EC
ω	Specific dissipation rate

References

1. Hepburn, C.; Adlen, E.; Beddington, J.; Carter, E.A.; Fuss, S.; Mac Dowell, N.; Minx, J.C.; Smith, P.; Williams, C.K. The technological and economic prospects for CO₂ utilization and removal. *Nature* **2019**, *575*, 87–97. [[CrossRef](#)]
2. Zhang, Z.; Pan, S.; Li, H.; Cai, J.; Olabi, A.G.; Anthony, E.J.; Manovic, V. Recent advances in carbon dioxide utilization. *Renew. Sustain. Energy Rev.* **2020**, *125*, 109799. [[CrossRef](#)]
3. Ronda-Lloret, M.; Rothenberg, G.; Shiju, N.R. A Critical Look at Direct Catalytic Hydrogenation of Carbon Dioxide to Olefins. *ChemSusChem* **2019**, *12*, 3896–3914. [[CrossRef](#)] [[PubMed](#)]
4. Guo, L.; Sun, J.; Ge, Q.; Tsubaki, N. Recent advances in direct catalytic hydrogenation of carbon dioxide to valuable C₂₊ hydrocarbons. *J. Mater. Chem. A* **2018**, *6*, 23244–23262. [[CrossRef](#)]
5. Yang, H.; Zhang, C.; Gao, P.; Wang, H.; Li, X.; Zhong, L.; Wei, W.; Sun, Y. A review of the catalytic hydrogenation of carbon dioxide into value-added hydrocarbons. *Catal. Sci. Technol.* **2017**, *7*, 4580–4598. [[CrossRef](#)]
6. Ye, K.; Zhou, Z.; Shao, J.; Lin, L.; Gao, D.; Ta, N.; Si, R.; Wang, G.; Bao, X. In Situ Reconstruction of a Hierarchical Sn-Cu/SnO_x Core/Shell Catalyst for High-Performance CO₂ Electroreduction. *Angew. Chem. Int. Ed.* **2020**, *59*, 4814–4821. [[CrossRef](#)]
7. Wu, C.; Lin, L.; Liu, J.; Zhang, J.; Zhang, F.; Zhou, T.; Rui, N.; Yao, S.; Deng, Y.; Yang, F.; et al. Inverse ZrO₂/Cu as a highly efficient methanol synthesis catalyst from CO₂ hydrogenation. *Nat. Commun.* **2020**, *11*, 5767. [[CrossRef](#)]
8. Pedersen, J.K.; Batchelor, T.A.A.; Bagger, A.; Rossmeis, J. High-Entropy Alloys as Catalysts for the CO₂ and CO Reduction Reactions. *ACS Catal.* **2020**, *10*, 2169–2176. [[CrossRef](#)]
9. Jiang, Z.; Wang, T.; Pei, J.; Shang, H.; Zhou, D.; Li, H.; Dong, J.; Wang, Y.; Cao, R.; Zhuang, Z.; et al. Discovery of main group single Sb–N₄ active sites for CO₂ electroreduction to formate with high efficiency. *Energy Environ. Sci.* **2020**, *13*, 2856–2863. [[CrossRef](#)]
10. Hu, J.; Yu, L.; Deng, J.; Wang, Y.; Cheng, K.; Ma, C.; Zhang, Q.; Wen, W.; Yu, S.; Pan, Y.; et al. Sulfur vacancy-rich MoS₂ as a catalyst for the hydrogenation of CO₂ to methanol. *Nat. Catal.* **2021**, *4*, 242–250. [[CrossRef](#)]
11. Wang, J.; Li, G.; Li, Z.; Tang, C.; Feng, Z.; An, H.; Liu, H.; Liu, T.; Li, C. A highly selective and stable ZnO-ZrO₂ solid solution catalyst for CO₂ hydrogenation to methanol. *Sci. Adv.* **2017**, *3*, e1701290. [[CrossRef](#)] [[PubMed](#)]
12. Sen, R.; Goepfert, A.; Kar, S.; Prakash, G.K.S. Hydroxide Based Integrated CO₂ Capture from Air and Conversion to Methanol. *J. Am. Chem. Soc.* **2020**, *142*, 4544–4549. [[CrossRef](#)] [[PubMed](#)]
13. Hartadi, Y.; Widmann, D.; Behm, R.J. CO₂ Hydrogenation to Methanol on Supported Au Catalysts under Moderate Reaction Conditions: Support and Particle Size Effects. *ChemSusChem* **2015**, *8*, 456–465. [[CrossRef](#)] [[PubMed](#)]
14. Frei, M.S.; Mondelli, C.; Cesarini, A.; Krumeich, F.; Hauert, R.; Stewart, J.A.; Curulla Ferré, D.; Pérez-Ramírez, J. Role of Zirconia in Indium Oxide-Catalyzed CO₂ Hydrogenation to Methanol. *ACS Catal.* **2020**, *10*, 1133–1145. [[CrossRef](#)]
15. Dang, S.; Qin, B.; Yang, Y.; Wang, H.; Cai, J.; Han, Y.; Li, S.; Gao, P.; Sun, Y. Rationally designed indium oxide catalysts for CO₂ hydrogenation to methanol with high activity and selectivity. *Sci. Adv.* **2020**, *6*, eaaz2060. [[CrossRef](#)] [[PubMed](#)]
16. Wang, W.; Wang, S.; Ma, X.; Gong, J. Recent advances in catalytic hydrogenation of carbon dioxide. *Chem. Soc. Rev.* **2011**, *40*, 3703–3727. [[CrossRef](#)]
17. Wang, S.; Zhao, L.; Wang, W.; Zhao, Y.; Zhang, G.; Ma, X.; Gong, J. Morphology control of ceria nanocrystals for catalytic conversion of CO₂ with methanol. *Nanoscale* **2013**, *5*, 5582–5588. [[CrossRef](#)]
18. Song, Q.; Zhou, Z.; He, L. Efficient, selective and sustainable catalysis of carbon dioxide. *Green Chem.* **2017**, *19*, 3707–3728. [[CrossRef](#)]
19. Tamura, M.; Kitanaka, T.; Nakagawa, Y.; Tomishige, K. Cu Sub-Nanoparticles on Cu/CeO₂ as an Effective Catalyst for Methanol Synthesis from Organic Carbonate by Hydrogenation. *ACS Catal.* **2016**, *6*, 376–380. [[CrossRef](#)]
20. Li, Y.; Junge, K.; Beller, M. Improving the Efficiency of the Hydrogenation of Carbonates and Carbon Dioxide to Methanol. *ChemCatChem* **2013**, *5*, 1072–1074. [[CrossRef](#)]
21. Du, X.; Sun, X.; Jin, C.; Jiang, Z.; Su, D.; Wang, J. Efficient Hydrogenation of Alkyl Formate to Methanol over Nanocomposite Copper/Alumina Catalysts. *ChemCatChem* **2014**, *6*, 3075–3079. [[CrossRef](#)]
22. Balaraman, E.; Gunanathan, C.; Zhang, J.; Shimon, L.J.W.; Milstein, D. Efficient hydrogenation of organic carbonates, carbamates and formates indicates alternative routes to methanol based on CO₂ and CO. *Nat. Chem.* **2011**, *3*, 609–614. [[CrossRef](#)] [[PubMed](#)]
23. Du, X.; Jiang, Z.; Su, D.; Wang, J. Research Progress on the Indirect Hydrogenation of Carbon Dioxide to Methanol. *ChemSusChem* **2016**, *9*, 322–332. [[CrossRef](#)] [[PubMed](#)]
24. Yu, B.-Y.; Chen, M.-K.; Chien, I.L. Assessment on CO₂ Utilization through Rigorous Simulation: Converting CO₂ to Dimethyl Carbonate. *Ind. Eng. Chem. Res.* **2018**, *57*, 639–652. [[CrossRef](#)]
25. Gu, X.; Zhang, X.; Zhang, X.; Deng, C. Simulation and assessment of manufacturing ethylene carbonate from ethylene oxide in multiple process routes. *Chin. J. Chem. Eng.* **2021**, *31*, 135–144. [[CrossRef](#)]
26. Han, Z.; Rong, L.; Wu, J.; Zhang, L.; Wang, Z.; Ding, K. Catalytic Hydrogenation of Cyclic Carbonates: A Practical Approach from CO₂ and Epoxides to Methanol and Diols. *Angew. Chem. Int. Ed.* **2012**, *51*, 13041–13045. [[CrossRef](#)]
27. Wu, X.; Ji, L.; Ji, Y.; Elageed, E.H.M.; Gao, G. Hydrogenation of ethylene carbonate catalyzed by lutidine-bridged N-heterocyclic carbene ligands and ruthenium precursors. *Catal. Commun.* **2016**, *85*, 57–60. [[CrossRef](#)]
28. Lian, C.; Ren, F.; Liu, Y.; Zhao, G.; Ji, Y.; Rong, H.; Jia, W.; Ma, L.; Lu, H.; Wang, D.; et al. Heterogeneous selective hydrogenation of ethylene carbonate to methanol and ethylene glycol over a copper chromite nanocatalyst. *Chem. Commun.* **2015**, *51*, 1252–1254. [[CrossRef](#)]

29. Zhang, M.; Yang, Y.; Li, A.; Yao, D.; Gao, Y.; Fayisa, B.A.; Wang, M.-Y.; Huang, S.; Lv, J.; Wang, Y.; et al. Nanoflower-like Cu/SiO₂ Catalyst for Hydrogenation of Ethylene Carbonate to Methanol and Ethylene Glycol: Enriching H₂ Adsorption. *ChemCatChem* **2020**, *12*, 3670–3678. [[CrossRef](#)]
30. Yang, Y.; Yao, D.; Zhang, M.; Li, A.; Gao, Y.; Fayisa, B.A.; Wang, M.; Huang, S.; Wang, Y.; Ma, X. Efficient hydrogenation of CO₂-derived ethylene carbonate to methanol and ethylene glycol over Mo-doped Cu/SiO₂ catalyst. *Catal. Today* **2021**, *371*, 113–119. [[CrossRef](#)]
31. Ding, Y.; Tian, J.; Chen, W.; Guan, Y.; Xu, H.; Li, X.; Wu, H.; Wu, P. One-pot synthesized core/shell structured zeolite@copper catalysts for selective hydrogenation of ethylene carbonate to methanol and ethylene glycol. *Green Chem.* **2019**, *21*, 5414–5426. [[CrossRef](#)]
32. Zhou, M.; Shi, Y.; Ma, K.; Tang, S.; Liu, C.; Yue, H.; Liang, B. Nanoarray Cu/SiO₂ Catalysts Embedded in Monolithic Channels for the Stable and Efficient Hydrogenation of CO₂-Derived Ethylene Carbonate. *Ind. Eng. Chem. Res* **2018**, *57*, 1924–1934. [[CrossRef](#)]
33. Chen, X.; Cui, Y.; Wen, C.; Wang, B.; Dai, W. Continuous synthesis of methanol: Heterogeneous hydrogenation of ethylene carbonate over Cu/HMS catalysts in a fixed bed reactor system. *Chem. Commun.* **2015**, *51*, 13776–13778. [[CrossRef](#)] [[PubMed](#)]
34. Li, F.; Wang, L.; Han, X.; Cao, Y.; He, P.; Li, H. Selective hydrogenation of ethylene carbonate to methanol and ethylene glycol over Cu/SiO₂ catalysts prepared by ammonia evaporation method. *Int. J. Hydrogen Energy* **2017**, *42*, 2144–2156. [[CrossRef](#)]
35. Chen, W.; Song, T.; Tian, J.; Wu, P.; Li, X. An efficient Cu-based catalyst for the hydrogenation of ethylene carbonate to ethylene glycol and methanol. *Catal. Sci. Technol.* **2019**, *9*, 6749–6759. [[CrossRef](#)]
36. Tian, J.; Chen, W.; Wu, P.; Zhu, Z.; Li, X. Cu–Mg–Zr/SiO₂ catalyst for the selective hydrogenation of ethylene carbonate to methanol and ethylene glycol. *Catal. Sci. Technol.* **2018**, *8*, 2624–2635. [[CrossRef](#)]
37. Song, T.; Qi, Y.; Jia, A.; Ta, N.; Lu, J.; Wu, P.; Li, X. Continuous hydrogenation of CO₂-derived ethylene carbonate to methanol and ethylene glycol at Cu–MoO_x interface with a low H₂/ester ratio. *J. Catal.* **2021**, *399*, 98–110. [[CrossRef](#)]
38. Chen, X.; Wang, L.; Zhang, C.; Tu, W.; Cao, Y.; He, P.; Li, J.; Li, H. The effective and stable Cu–C@SiO₂ catalyst for the syntheses of methanol and ethylene glycol via selective hydrogenation of ethylene carbonate. *Int. J. Hydrogen Energy* **2021**, *46*, 17209–17220. [[CrossRef](#)]
39. Deng, F.; Li, N.; Tang, S.; Liu, C.; Yue, H.; Liang, B. Evolution of active sites and catalytic consequences of mesoporous MCM-41 supported copper catalysts for the hydrogenation of ethylene carbonate. *Chem. Eng. J.* **2018**, *334*, 1943–1953. [[CrossRef](#)]
40. Poels, E.K.; Brands, D.S. Modification of Cu/ZnO/SiO₂ catalysts by high temperature reduction. *Appl. Catal. A: Gen.* **2000**, *191*, 83–96. [[CrossRef](#)]
41. Meyer, J.J.; Tan, P.; Apfelbacher, A.; Daschner, R.; Hornung, A. Modeling of a Methanol Synthesis Reactor for Storage of Renewable Energy and Conversion of CO₂—Comparison of Two Kinetic Models. *Chem. Eng. Technol.* **2016**, *39*, 233–245. [[CrossRef](#)]
42. Bozzano, G.; Manenti, F. Efficient methanol synthesis: Perspectives, technologies and optimization strategies. *Prog. Energy Combust. Sci.* **2016**, *56*, 71–105. [[CrossRef](#)]
43. Haid, J.; Koss, U. Lurgi's Mega-Methanol technology opens the door for a new era in down-stream applications. In *Studies in Surface Science and Catalysis*; Iglesia, E., Spivey, J.J., Fleisch, T.H., Eds.; Elsevier Science Pub. Co. Inc.: Amsterdam, The Netherlands, 2001; Volume 136, pp. 399–404.
44. Samimi, F.; Feilzadeh, M.; Ranjbaran, M.; Arjmand, M.; Rahimpour, M.R. Phase stability analysis on green methanol synthesis process from CO₂ hydrogenation in water cooled, gas cooled and double cooled tubular reactors. *Fuel Processing Technol.* **2018**, *181*, 375–387. [[CrossRef](#)]
45. Cui, X.; Kær, S.K. A comparative study on three reactor types for methanol synthesis from syngas and CO₂. *Chem. Eng. J.* **2020**, *393*, 124632. [[CrossRef](#)]
46. Kuo, K.K. *Principles of Combustion*; Elsevier Science Pub. Co. Inc.: Amsterdam, The Netherlands, 1986.
47. Verman, L.C.; Banerjee, S. Effect of Container Walls on Packing Density of Particles. *Nature* **1946**, *157*, 584. [[CrossRef](#)]
48. Theuerkauf, J.; Witt, P.; Schwesig, D. Analysis of particle porosity distribution in fixed beds using the discrete element method. *Powder Technol.* **2006**, *165*, 92–99. [[CrossRef](#)]
49. Roshani, S. *Elucidation of Local and Global Structural Properties of Packed Bed Configurations*; The University of Leeds: Leeds, UK, 1990.
50. de Klerk, A. Voidage variation in packed beds at small column to particle diameter ratio. *AIChE J.* **2003**, *49*, 2022–2029. [[CrossRef](#)]
51. Ergun, S. Fluid Flow Through Packed Columns. *Chem. Eng. Prog.* **1952**, *48*, 89–94.
52. Koning, B. *Heat and Mass Transport in Tubular Packed Bed Reactors at Reacting and Non-Reacting Conditions*; University of Twente: Enschede, The Netherlands, 2002.
53. Agnew, J.B.; Potter, O. Heat transfer properties of packed tubes of small diameter. *Trans. Inst. Chem. Eng.* **1970**, *48*, T15.
54. Bauer, R.; Schluender, E.U. Effective Radial Thermal Conductivity of Packings in Gas Flow-1. Convective Transport Coefficient. *Int. Chem. Eng.* **1978**, *18*, 181–188.
55. Bauer, R.; Schluender, E.U. Effective Radial Thermal Conductivity of Packings in Gas Flow-2. Thermal Conductivity of the Packing Fraction without Gas Flow. *Int. Chem. Eng.* **1978**, *18*, 189–204.
56. Westerterp, K.R.; Swaaij, W.P.M.V.; Beenackers, A.A.C.M. *Chemical Reactor Design and Operation*, 2nd ed.; John Wiley & Sons, Ltd.: Hoboken, NJ, USA, 1987; p. 800.
57. Fahien, R.W.; Smith, J.M. Mass transfer in packed beds. *AIChE J.* **1955**, *1*, 28–37. [[CrossRef](#)]
58. Specchia, V.; Baldi, G.; Sicardi, S. Heat transfer in packed bed reactors with one phase flow. *Chem. Eng. Commun.* **1980**, *4*, 361–380. [[CrossRef](#)]

59. Wakao, N.; Funazkri, T. Effect of fluid dispersion coefficients on particle-to-fluid mass transfer coefficients in packed beds: Correlation of sherwood numbers. *Chem. Eng. Sci.* **1978**, *33*, 1375–1384. [[CrossRef](#)]
60. Bai, P.T.; Manokaran, V.; Saiprasad, P.S.; Srinath, S. Studies on Heat and Mass Transfer Limitations in Oxidative Dehydrogenation of Ethane Over Cr₂O₃/Al₂O₃ Catalyst. *Procedia Eng.* **2015**, *127*, 1338–1345. [[CrossRef](#)]
61. Soomro, M.; Hughes, R. The thermal conductivity of porous catalyst pellets. *Can. J. Chem. Eng.* **1979**, *57*, 24–28. [[CrossRef](#)]
62. McCabe, W.L.; Smith, J.C.; Harriott, P. Heat Transfer to Fluids without Phase Change. In *Unit Operations in Chemical Engineering*; Clark, B.J., Castellano, E., Eds.; McGraw Hill, Inc.: New York, NY, USA, 1993; pp. 647–685.
63. Ross, J.R.H. Chapter 8-Mass and Heat Transfer Limitations and Other Aspects of the Use of Large-Scale Catalytic Reactors. In *Contemporary Catalysis*; Ross, J.R.H., Ed.; Elsevier Science Pub. Co. Inc.: Amsterdam, The Netherlands, 2019; pp. 187–213.
64. Plessis, J.P.; Diedericks, G. Fluid transport in porous media: Pore-scale modelling of interstitial transport phenomena. *Comput. Mech. Publ.* **1997**, *11*, 61–104.
65. Bird, R.B.; Stewart, W.E.; Lightfoot, E.N. *Transport Phenomena*; John Wiley & Sons, Ltd.: New York, NY, USA, 1960.